

# 1 Sea-surface temperature variability and climate drivers in 2 Cuba's Jardines de la Reina National Park (2003–2022)

3  
4 Maibelin Castillo-Alvarez<sup>1,2</sup>; Oscar Pizarro<sup>2,3</sup>; Alain Muñoz-Caravaca<sup>4</sup>; Iván Pérez-Santos<sup>5,6</sup>;  
5 David Carrasco<sup>2</sup>; David Francisco Bustos-Usta<sup>1,6</sup>; Laura Castellanos-Torres<sup>1,2,4</sup>

6  
7 <sup>1</sup> Postgraduate Program in Oceanography, Department of Oceanography, Faculty of Natural Sciences and  
8 Oceanography. Universidad de Concepción, Chile.

9 <sup>2</sup> Millennium Institute of Oceanography (IMO), Universidad de Concepción, Chile.

10 <sup>3</sup> Department of Geophysics, Universidad de Concepción, Chile.

11 <sup>4</sup> Centro de Estudios Ambientales de Cienfuegos. AP 5, 59350, Ciudad Nuclear, Cienfuegos, Cuba.

12 <sup>5</sup> Centro i-mar, Universidad de los Lagos, Puerto Montt 5480000, Chile

13 <sup>6</sup> Center for Oceanographic Research COPAS Sur-Austral and COPAS COASTAL (FB210021), Universidad  
14 de Concepción, Chile.

15  
16  
17 *Correspondence to:* [mcastilloa@udec.cl](mailto:mcastilloa@udec.cl) and [opizarro@udec.cl](mailto:opizarro@udec.cl)

18  
19 **Abstract.** Coral reef systems on the southeastern Cuban shelf are exposed to rapid warming and increasingly  
20 frequent marine heatwaves (MHWs). However, the physical drivers of local sea-surface temperature (SST)  
21 variability remain poorly quantified. The present study examines seasonal-to-decadal SST variability in and  
22 around the Jardines de la Reina National Park (JRNP) and investigates the extent to which atmospheric–ocean  
23 processes and large-scale climate modes influence that variability. The study analyses daily 1-km Multi-Scale  
24 Ultra High Resolution (MUR) SST from 2003–2022, in conjunction with ERA5 surface heat fluxes and  
25 GLORYS12 mixed-layer fields. A mixed-layer heat budget, compiled from daily values and averaged to  
26 monthly values, is used to attribute the seasonal cycle; long-term trends, MHWs and modes of variability  
27 (Orthogonal Functions) can be used to explain interannual to decadal changes and their links to El Niño  
28 Southern Oscillation (ENSO), the Western Hemisphere Warm Pool (WHWP), the Tropical North Atlantic  
29 (TNA) and the North Atlantic Oscillation (NAO).

30 Net air–sea heat exchange sets the seasonal evolution of SST, whereby horizontal advection provides a smaller  
31 modulation near the shelf break; a characteristic ~2-month lead of heat flux over temperature is consistent with  
32 mixed-layer heat storage. This thermodynamic control explains a marked autumn–winter shelf–offshore  
33 contrast between the shallow gulfs (Gulfs of Ana María and Guacanayabo) and the adjacent Caribbean Sea.  
34 Superimposed over this area is a warming trend of ~0.28°C decade<sup>-1</sup> (strongest in winter/transition months,  
35 peaking around April at ~0.48°C and November at ~0.35°C decade<sup>-1</sup>) and a step-like shift in 2011–2013 towards  
36 a persistently warmer state. MHWs intensified during the second decade; the mean event-wise maximum  
37 intensity was higher inside GAM, while upper categories occurred more frequently offshore. EOF1 (87.5%) is  
38 a basin-wide mode linked on an interannual basis to ENSO/WHWP and latent-heat flux and at low frequency  
39 to the NAO, while EOF2 (6.2%) captures a shelf–offshore dipole related to TNA.

40 The aforementioned Our results provide a physical basis for which to issue early warnings from forecasts of net  
41 heat flux and mixed-layer depth, thus encouraging the use of regional high-resolution modeling and targeted  
42 observations. Key limitations to the present study include a 20-year MHW baseline and an under-resolution of  
43 currents in highly shallow and complex bathymetry.

## 44 1. Introduction

45 Sea surface temperature (SST) is a key regulator of marine ecosystems, since it drives physical, chemical and  
46 biological processes. Its variability has profound implications for coastal and oceanic regions in a warming  
47 climate (Venegas et al., 2023). Since the industrial era, anthropogenic pressures have altered ocean dynamics  
48 and accelerated habitat degradation (Jackson et al., 2014; Lotze et al., 2006). Rising SSTs are closely linked to  
49 coral bleaching, habitat fragmentation and biodiversity loss in tropical regions (Bruno et al., 2019; Hughes et  
50 al., 2003). Coral reef ecosystems are susceptible to temperature fluctuations and to co-occurring stressors,  
51 including light, sedimentation and chemical changes (Cramer et al., 2020). As a result, understanding the  
52 patterns and drivers of SST variability has become crucial in order to predict ecological impacts and inform  
53 conservation efforts.

54 The Caribbean Sea (CS) hosts extensive coral reefs and numerous marine protected areas (MPAs), which are  
55 central to regional conservation and livelihoods. The Jardines de la Reina National Park (JRNP), the largest  
56 marine reserve in Cuba and one of the largest in the Caribbean, is notable due to its exceptional reef conditions  
57 and biodiversity (Appeldoorn and Lindeman, 2003; Linton et al., 2002; Gerhartz-Muro et al., 2018). Yet, JRNP  
58 faces a number of challenges typical of Caribbean reefs, including the dramatic decline of historically dominant  
59 species, such as *Acropora palmata*, now classified as critically endangered (Caballero-Aragón et al., 2020).  
60 Prior work at JRNP has focused primarily on reef ecology and conservation status (Hernández-Fernández et al.,  
61 2011, 2016, 2019a; Pina-Amargós et al., 2011), with fewer studies addressing the physical drivers that modulate  
62 local thermal stress and ecosystem vulnerability. This research gap is significant, since thermal extremes and  
63 the persistence thereof increasingly govern the risk of coral bleaching across the region (van Hooidek et al.,  
64 2015; Graham et al., 2015; Mumby et al., 2014).

65 At a broader scale, southern Cuba exhibits warmer SST than the northern shelf of the island, influenced by  
66 exchanges with the CS (Cerqueira-Estrada et al., 2005; Chollett et al., 2012; Caravaca et al., 2022; González-De  
67 Zayas et al., 2022). Basin-wide analyses also point to a significant warming trend during recent decades, which  
68 are particularly pronounced to the south of Cuba (Avila-Alonso et al., 2020). However, existing studies provide  
69 merely a partial view of SST variability on the southeastern Cuban shelf and seldom disentangle the relative  
70 roles of air-sea heat fluxes, horizontal advection and large-scale climate modes in shaping local conditions  
71 within and adjacent to JRNP.

72 Large-scale atmospheric variability modulates Caribbean SST through several well-documented pathways. The  
73 El Niño Southern Oscillation (ENSO) influences trade winds and latent heat flux over the Western Hemisphere  
74 Warm Pool (WHWP), defined as the region warmer than 28.5°C in the Western Tropical Atlantic and in the

75 eastern North Pacific, which alter regional SST at interannual scales (Wang and Enfield, 2001, 2003; Czaja et  
76 al., 2002). The North Atlantic Oscillation (NAO) affects wind patterns, precipitation and heat exchange across  
77 the North Atlantic–Caribbean system, including via the Caribbean Low-Level Jet (Hurrell, 1995; Wang et al.,  
78 2007; Cook & Vizu, 2010). Additional variability arises from the Tropical North Atlantic (TNA) and WHWP  
79 indices, which capture shifts in regional SST (Enfield et al., 1999; Enfield and Lee, 2005). The process of  
80 clarifying how these climate modes project onto local SST in the shelf versus adjacent oceanic waters near  
81 JRNP is crucial for efforts to link physical forcing with ecological risk.

82 In the present study, ~~wethe authors~~ investigate seasonal-to-decadal variability of sea-surface temperature in and  
83 around JRNP and its controlling mechanisms using daily 1-km Multi-Scale Ultra High Resolution (MUR) SST  
84 (2003–2022), ERA5 dataset surface heat fluxes, and GLORYS12 (1/12°) dataset currents/temperature by: (i)  
85 resolving the seasonal cycle and diagnosing the mixed-layer heat budget to gauge air–sea heat exchange versus  
86 horizontal advection; (ii) quantifying long-term trends and testing for regime shifts; (iii) detecting and  
87 characterizing marine heatwaves (MHWs); and (iv) extracting dominant modes via Empirical Orthogonal  
88 Functions (EOFs) and relating them to the El Niño–Southern Oscillation, the North Atlantic Oscillation, the  
89 Tropical North Atlantic, and the Western Hemisphere Warm Pool.

90 Accordingly, ~~we the authors of the present research~~ address three working hypotheses: (1) at seasonal scales,  
91 air–sea heat fluxes dominate SST variability, with shallow shelf waters exhibiting stronger amplitude and faster  
92 cooling/warming than adjacent oceanic waters; (2) interannual variability shows modulation by ENSO/WHWP  
93 and TNA via latent-heat-flux anomalies and circulation changes; and (3) decadal changes in the region,  
94 including post-2010 regime shifts, are consistent with NAO-related variations in atmospheric forcing. By  
95 resolving shelf–offshore contrasts and attributing variability across time scales, the analysis herein provides a  
96 physical basis for interpreting recent and future thermal stress in this MPA in addition to anticipating ecosystem  
97 responses under continued warming.

## 98 **2. Data and methods**

### 99 **2.1 Study region: Jardines de la Reina National Park (JRNP)**

100 The JRNP lies on the southeastern Cuban shelf, bordered to the north by the Gulf of Ana María (GAM), to the  
101 east by the Gulf of Guacanayabo (GG) and to the south by the CS (Figure 1). The archipelago comprises ~661  
102 cays (keys) that extend east–west and which are fringed by mangroves. According to Pina Amargós et al.  
103 (2011), the protected area covers 217,036 ha, of which 200,957 ha are marine hectares. The seafloor shows a  
104 marked north–south contrast: to the north, the shallow GAM is characterized by extensive flat banks, seagrass  
105 beds and soft sediment with a general depth of < 20 m; to the south, the shelf edge transitions abruptly to a steep  
106 continental slope descending to > 3,000 m. This sharp gradient underpins a mosaic of habitats, from shallow  
107 coastal ecosystems to deep-sea environments.

108 The region has a tropical climate with two boreal seasons: a wet season (May–October) and a dry season  
109 (November–April). Prevailing trade winds are generally northeasterly and strengthen during the dry season

110 (Pérez-Santos et al., 2010). Sea-level pressure follows a seasonal cycle, with higher values in boreal winter  
111 (January–March) under the influence of the subtropical high, and lower values in summer (July–September) as  
112 the intertropical convergence zone approaches (Waliser and Jiang, 2015). Air temperatures are warm year-  
113 round (~24–30°C) and there is modest interannual variability, despite pronounced diurnal and seasonal cycles.  
114 Summer is warmest while winter is slightly cooler (Caravaca et al., 2022). On the southeastern Cuban shelf, the  
115 mean flow is westward under the prevailing easterlies (Emilsson and Tápanes, 1971). It is modulated by tides  
116 and currents from the adjacent ocean, notably the Caribbean Current -Arriaza et al., 2008). Tides are mixed ~~and~~  
117 ~~microtidal~~, and exert little direct control on the mean shelf circulation, although tidal currents can enhance  
118 vertical mixing (Emilsson and Tápanes, 1971; Arriaza et al., 2008).

## 119 2.2 SST data

120 Sea-surface temperature was obtained from the Group for High Resolution Sea Surface Temperature -MUR  
121 Level-4 analysis produced by the NASA Jet Propulsion Laboratory. This product provides daily global fields  
122 at ~1 km (0.01°) by blending multiple infrared and microwave satellite sensors (Chin et al., 2017) and is widely  
123 used in tropical reef and coastal studies (for example, Kumagai and Yamano, 2018; Skerrett et al., 2024). The  
124 present study analyzed data from 2003 to 2022 and subsequently subset the domain, as shown in Figure 1.

125 All processing was performed on the native 1km grid, unless otherwise specified. Daily fields were: (i) land-  
126 masked and quality-screened using the product masks; (ii) averaged to monthly means for the long-term,  
127 seasonal and EOF analyses; and (iii) converted to monthly anomalies by removing the 2003–2022 monthly  
128 climatology (further details are provided in Section 2.5). For diagnostics requiring co-location with reanalyses  
129 (mixed-layer heat budget and horizontal advection), SST was bilinearly remapped to the target grid  
130 (GLORYS12 at 1/12° or ERA5 at 1/4°) to avoid artificial gradients from mismatched resolutions. All  
131 temperatures are reported in °C.

132 ~~The authors of the present research-We~~ retained the 1-km fields to ~~showdepict~~ frontal structures in Figure 2;  
133 frontal overlays are computed from local SST differences (threshold  $\geq 0.5^\circ\text{C}$ ) and lightly smoothed with a 3×3  
134 neighbourhood operator to suppress pixel-scale noise.

135 It should be noted that MUR SST was not used in the mixed-layer heat budget (Section 2.6); there, ~~authors we~~  
136 diagnosed temperature tendencies ( $\partial T/\partial t$ ) using the GLORYS12 mixed-layer temperature (MLT), depth and  
137 currents for reasons of internal consistency with regards to the terms. At monthly scales, MUR SST and  
138 GLORYS12 MLT were correlated throughout the study area, thus, variability in MLT is interpreted as the  
139 explanation for the observed SST variability.

140 To assess the internal consistency of the SST variability represented by the different products used in this study,  
141 we performed a quantitative intercomparison between MUR SST, ERA5 SST, and GLORYS12 mixed-layer  
142 temperature (MLT) over the full analysis domain and period (2003–2022). The agreement is summarized in  
143 Supplementary Note 1 and Figure S1 using a Taylor diagram (correlation, normalized standard deviation, and  
144 cantered RMSD referenced to MUR), which provides an objective measure of how well the coarser-resolution

145 products reproduce the temporal variability and amplitude of the satellite-based SST anomalies. In addition, an  
146 independent consistency check using short-term in situ temperature time-series available within the Jardines de  
147 la Reina region is presented in Supplementary Figure S2. Although these comparisons do not constitute a full  
148 in situ validation for the region, they support the suitability of MUR SST for describing spatial and temporal  
149 variability and provide a transparent characterization of cross-product differences relevant to the interpretation  
150 of our results.

### 151 **2.3 Atmospheric fluxes (ERA5) and ocean reanalysis (GLORYS12)**

152 The present study used ERA5 surface flux components (shortwave, longwave, latent and sensible) and 10 m  
153 winds at native hourly resolution, aggregated to daily and then monthly means for the period 2003–2022. The  
154 upper-ocean state was characterized with GLORYS12 at daily resolution (temperature, horizontal currents and  
155 Ocean Mixed Layer Thickness), with monthly means used for non-budget diagnostics. Heat flux was measured  
156 in  $W\ m^{-2}$ . The oceanographic convention that holds that positive net heat flux warms the ocean was adopted  
157 throughout the course of the present research.

158 The upper-ocean state was characterized by GLORYS12 (eddy-resolving,  $1/12^\circ$ , 50 vertical levels, daily), from  
159 which potential temperature, horizontal currents and mixed layer depth and temperature were extracted over  
160 the same period. Fields were subset to the domain shown in Figure 1 and, where necessary, bilinearly remapped  
161 to a standard grid (ERA5-GLORYS12) for the mixed-layer heat budget and advection diagnostics. Regarding  
162 the budget, ERA5 fluxes were first aggregated to daily values and then bilinearly remapped to the GLORYS12  
163 grid; the results were subsequently averaged to a monthly basis. For descriptive analyses, monthly fields were  
164 utilized.

### 165 **2.4 Climate indices**

166 The present study used a monthly time series of large-scale climate indices known to modulate Caribbean SST.  
167 The ENSO was represented by the Multivariate ENSO Index v2 (MEI.v2) (Zhang et al., 2019; Wolter, 1993),  
168 obtained from the NOAA Physical Sciences Laboratory (PSL). The WHWP index (Wang and Enfield, 2001,  
169 2003; Enfield and Lee, 2005; Wang et al., 2006) and the TNA index (Enfield et al., 1999; Chen et al., 2021)  
170 were also taken from NOAA PSL. The NAO index was obtained from the NOAA Climate Prediction Center  
171 (CPC) (Barnston and Livezey, 1987; Chen and Van den Dool, 2003; Van den Dool et al., 2000).

172 All indices were analyzed at monthly resolution pertaining to the period 2003–2022, to match the SST analysis  
173 period. Prior to correlation and filtering analyses (Section 2.9), each index was standardized (zero mean, unit  
174 variance) over the 2003–2022 period. Provider sign conventions were retained.

175 ~~Data access notes: MEI.v2 and the WHWP/TNA indices were retrieved from the NOAA PSL portals; the NAO~~  
176 ~~index was retrieved from NOAA CPC (accessed in 2024–2025; URLs listed in the Data Availability statement).~~

### 177 **2.5 Statistical analysis**

178 All analyses were performed over the domain 19–21.75° N, 77–80° W (Figure 1). Land points were masked.  
179 Daily fields were aggregated to monthly means, while monthly anomalies were computed by removing the  
180 2003–2022 monthly climatology. Unless otherwise specified, statistics refer to the aforementioned monthly  
181 anomalies.

182 Long-term monthly means were used to show the seasonal cycle of SST and surface heat fluxes (Figures 2–4).  
183 ~~SST frontal zones shown in Figure 2 were identified from local SST differences with a  $\geq 0.5^\circ\text{C}$  threshold and~~  
184 ~~lightly smoothed with a  $3\times 3$  neighbourhood operator to suppress short wavelength (pixel scale) noise.~~

185 To contrast shelf and offshore regimes, ~~we the authors~~ computed time series over the two small boxes shown in  
186 Figure 1: GAM (shelf) and CS (oceanic). For each box, monthly anomalies, standard deviations and seasonal  
187 composites were calculated. To verify that our GAM and CS time series are not sensitive to the exact choice of  
188 box location and size, we repeated the analysis using multiple alternative boxes within GAM and offshore in  
189 the CS (Note S2 and Figure S3 in the supplementary material). The resulting SST-anomaly time series remain  
190 highly consistent with the reference series (all correlations significant at  $\geq 95\%$  confidence; Table S1), indicating  
191 that the reported shelf–offshore contrasts are robust to reasonable variations in box definition.

192 Linear trends were estimated using ordinary least squares applied to monthly anomalies at each grid point,  
193 separately for each calendar month. Slopes are reported in  $^\circ\text{C}/\text{decade}^{-1}$ . Statistical significance was assessed at  
194 the 95% level using a two-sided Student’s t-test. To account for serial autocorrelation inherent in geophysical  
195 time series (“red noise”), which usually inflates nominal significance, we calculated the effective degrees of  
196 freedom ( $N^*$ ) following the approximation by Thomson and Emery (2024).  $N^*$  was estimated using the lag-1  
197 autocorrelation coefficient ( $r_1$ ):

$$N^* = N \frac{1 - |r_1|}{1 + |r_1|}$$

198 Thus, the significance tests for trends and correlations use an effective degrees-of-freedom estimate, yielding  
199 more conservative  $p$ -values under serial correlation. ~~ensure that the trend and correlation  $p$ -values represent~~  
200 independent realizations rather than persistence.

201 ~~Statistical significance was assessed at the 95% level using a two-sided t test with an effective sample size that~~  
202 ~~accounts for autocorrelation in the time series (for example, Thomson and Emery, 2024).~~

203  
204 To quantify coupling between SST and different drivers, cross-correlations between SST anomalies and net  
205 surface heat flux were computed (and, where relevant, horizontal heat advection; Section 2.6) using monthly  
206 data, by scanning lags from  $-6$  to  $+6$  months. Reported lags correspond to the peak absolute correlation.  
207 Significance was evaluated using the t-test for the correlation coefficient and the effective degrees of freedom  
208 approach. Where budget terms are summed (Section 2.6; Figure 5), the uncertainty of the sum was obtained by  
209 root-sum-of-squares, assuming weak covariance between terms at monthly resolution. All computations and  
210 figure generation were carried out via the MATLAB computing platform using standard scientific libraries.

## 211 2.6 Mixed-layer heat budget

212 To identify the processes governing the seasonal variability of SST, ~~we the authors~~ applied a standard  
 213 mixed-layer (ML) heat budget (for example, Moisan and Niiler, 1998). Since the budget is defined in  
 214 relation to the bulk mixed layer, the GLORYS12 MLT and mixed-layer depth (MLD) were used to  
 215 ensure physical and numerical consistency among terms (flux  $\rightarrow$  heating rate via  $h$ ; advection using  
 216 currents acting on the same temperature field). At monthly scales, MUR SST and GLORYS12 MLT were  
 217 well correlated over the domain (Section 2.2), Therefore, accounting for MLT variability was taken as  
 218 providing an explanation for the observed SST variability.

219 The prognostic equation for ML temperature  $T$  is

220

$$221 \quad \frac{\partial T}{\partial t} = \frac{Q_{net}}{\rho C_p h} - \mathbf{U} \cdot \nabla T - \frac{(\frac{\partial h}{\partial t} + u_{-h} \nabla h + w_{-h}) \Delta T}{h} + R,$$

222

223 where  $\rho = 1025 \text{ kg m}^{-3}$  is seawater density,  $C_p = 3990 \text{ J kg}^{-1} \text{ K}^{-1}$  is the specific heat capacity,  $h$  is the MLD,  
 224  $Q_{net}$  is the net downward surface heat flux (into the ocean,  $\text{W m}^{-2}$ ),  $\mathbf{U} = (U, V)$  is the horizontal current vector  
 225 representative of the ML. ~~The entrainment (positive downward) velocity at the ML base it is calculated as~~  
 226 ~~follows. The term  $u_{-h} \nabla h$  represents the contribution to vertical advection associated with horizontal flow moving~~  
 227 ~~over an inclined bottom, where  $u_{-h}$  is the horizontal velocity evaluated at the bottom and  $\nabla h$  the horizontal~~  
 228 ~~gradient of the bathymetry.  ~~$w_{-h}$  is obtained by vertically integrating the horizontal velocity divergence from~~~~  
 229  ~~$-h$  to the surface. is the entrainment (positive downward) velocity at the ML base,  $\Delta T = T_{ML} - T_{below}$  is the~~  
 230 temperature jump across the base of the ML, and  $R$  collects unresolved terms (for example, diffusion, sub-  
 231 monthly variability and analysis noise). All heating rates are reported in  $^{\circ}\text{C day}^{-1}$ . Conversion from flux to  
 232 heating rate follows, whereby

233

$$234 \quad 1 \text{ W m}^{-2} \equiv \frac{86400}{\rho C_p h} \text{ K day}^{-1},$$

235

236 so, for example, with  $h = 20 \text{ m}$ ,  $1 \text{ W m}^{-2} \sim 0.0011^{\circ}\text{C day}^{-1}$ .

237 All budget terms were computed from daily fields and then averaged to monthly means for analysis and  
 238 plots. MLD  $h$  was obtained from GLORYS12 “mixed layer thickness”. This estimate is based on a density  
 239 criterion ( $\Delta\sigma\theta = 0.03 \text{ kg m}^{-3}$ ), following the approach proposed by de Boyer Montégut et al. (2004). Daily  
 240 horizontal velocities from GLORYS12 were vertically averaged from the surface to the local ML base,  
 241 approximated by thickness-weighted averaging across GLORYS12 levels within the ML.

242 Surface fluxes ( $Q_{net}$ ) were estimated from ERA5 shortwave (SW) and longwave (LW) radiation, latent (LHF)  
 243 and sensible (SHF) heat fluxes on the  $1/4^{\circ}$  grid. To reiterate, ~~we the authors~~ adopted herein the oceanographic

244 convention that positive  $Q_{\text{net}}$  warms the ocean:  $Q_{\text{net}} = (\text{SW}\downarrow - \text{SW}\uparrow) + (\text{LW}\downarrow - \text{LW}\uparrow) - \text{LHF} - \text{SHF}$ . The  
245 ERA5 native signs (upward positive for turbulent fluxes) are converted accordingly. Fluxes were bilinearly  
246 remapped to the GLORYS12 grid prior to the application of Equation (1).

247 Horizontal gradients  $\partial T/\partial x$ ,  $\partial T/\partial y$  were computed with centered finite differences on the GLORYS12 grid. At  
248 a monthly resolution, the flux and advection tendencies in addition to their sum are presented. Furthermore, the  
249 entrainment plus unresolved tendency is treated as a residual (for example, the difference between the observed  
250 monthly MLT tendency and the sum of resolved terms).

## 251 **2.7 Marine heatwaves**

252 MHWs were detected from daily 1-km MUR SST data, following the hierarchical definition provided by  
253 Hobday et al. (2016, 2018), which contends that an MHW occurs when SST exceeds the seasonally varying  
254 90th percentile threshold for  $\geq 5$  consecutive days. For each grid point, ~~the authors of the present paper~~  
255 computed a day-of-year (DOY) climatology and corresponding 90th percentile threshold over the period 2003–  
256 2022. The DOY climatology and threshold were formed using a  $\pm 5$ -day moving window in order to smooth  
257 sampling noise. Events were characterized according to their intensity (absolute anomaly relative to the DOY  
258 climatology), duration, frequency, total MHW days and cumulative intensity. MHW categories  
259 (Moderate/Strong/Severe/Extreme) were assigned using the factor-of-rule relative to the local threshold  
260 exceedance (Hobday et al., 2018).

261 All diagnostics were computed per grid cell and subsequently summarized for the sub-regions (GAM and CS,  
262 Figure 1). Figure 8 shows the following: (i) maps pertaining to the mean maximum intensity and total MHW  
263 days (2003–2022); and (ii) an annual time series of the number of events, mean maximum intensity and  
264 maximum category for GAM and CS. It should be noted that the 20-year baseline (2003–2022) used in the  
265 present study corresponds to the period during which 1-km MUR SST data were available. Although shorter  
266 than the conventional 30-year climatology, the present research does, nevertheless, provide consistent  
267 thresholds across the study period. Schlegel et al. (2019) evaluated the impact of time-series length on MHW  
268 detection and found that, in general, event durations and intensities derived from a 10-year baseline are not  
269 appreciably different from those obtained using a standard 30-year baseline. In addition, to quantify the  
270 influence of our 20-year baseline and improve comparability with studies using 30-year climate normals, we  
271 performed a sensitivity analysis using GLORYS12, which provides a 30-year record (1993–2022). Following  
272 the Hobday et al. MHW definition, we computed MHW thresholds using a 30-year baseline (1993–2022) from  
273 GLORYS12 and re-detected MHWs over 2003–2022, then compared the number of days with MHW per year,  
274 mean intensity and the standard deviation of the intensity. Results are shown in Table S2. Differences were  
275 relatively small, indicating that our conclusions regarding the increase in MHWs during the second decade and  
276 the spatial contrasts within JRNP are not sensitive to baseline choice.

## 277 **2.8 Empirical orthogonal functions**

278 The present study used EOFs to extract the dominant space–time patterns of SST variability over the study  
279 domain (19–21.75° N, 77–80° W). The input field was monthly MUR SST anomalies (Section 2.2), i.e.,  
280 monthly means with the 2003–2022 monthly climatology ~~and trend~~ removed. Unless otherwise specified,  
281 anomalies time series were not detrended to ensure that the modes were able to capture the interannual–decadal  
282 variability previously discussed in Section 3.4. For comparison, we also include EOF results computed after  
283 removing the linear trend (Figure S4).~~It should be noted that a sensitivity test that not removed a linear trend~~  
284 ~~produced similar leading modes (not shown herein).~~ All calculations were performed on the native ~1 km grid.  
285 EOFs were obtained from the covariance matrix of the anomalies, computed via singular-value decomposition.  
286 Spatial patterns (EOFs) were scaled to the unit variance of their associated principal components (PCs) and the  
287 fraction of total variance explained by each mode. The sampling uncertainty of eigenvalues was estimated using  
288 North’s rule of thumb, and whereby modes were treated as distinct when the eigenvalue separation exceeded  
289 such uncertainty. PCs were standardized to zero mean and unit variance; their sign was arbitrary and was chosen  
290 so that positive EOF loadings corresponded to positive PC anomalies during warm events. For correlation  
291 analyses in Section 3.5, both the raw monthly PCs and low-pass filtered PCs were used to isolate variability  
292 bands. Specifically, a 2-year cutoff was employ~~ed by the authors~~ to emphasize interannual variability  
293 (ENSO/WHWP/TNA) and a 5-year cutoff for decadal/interdecadal variability (NAO). EOF analysis was carried  
294 out in MATLAB using standard linear-algebra routines.

## 295 **3. Results**

### 296 **3.1 Seasonal cycle and mixed-layer heat budget (GAM vs CS)**

#### 297 **3.1.1 SST and flux climatologies**

298 Monthly SST climatologies (Figure 2) exhibited the expected annual cycles, with boreal summer–early autumn  
299 (August–September) temperatures reaching ~30–33 °C, and winter (January–March) readings dropping to ~22–  
300 26 °C. A pronounced shelf–offshore contrast emerged from November to March, when the GAM/GG shallow  
301 waters are cooler than the adjacent CS, while from April to October this contrast weakened and wase virtually  
302 absent in certain months (for example, April and September–October). SST fronts ( $\geq 0.5$  °C) aligned with the  
303 shelf edge and were most frequent/intense during the transition and winter months, consistent with stronger  
304 horizontal gradients at that time.

305 Air–sea flux climatologies (Figure 3) indicated net ocean cooling from October to March and net warming from  
306 April to September. Winter cooling was strongest within the gulf, whereas summer heat peaked near the shelf  
307 break and CS. Cross-correlations between SST and net heat flux reveal a high degree of coupling ( $R^2_r \approx$ between  
308 0.6–0.9), with a characteristic lag of ~2 months (flux leads SST; see Figure S5), consistent with mixed-layer  
309 heat storage. Seasonal maps of horizontal heat advection (Figure 4) reveal smaller-magnitude, spatially patchy  
310 tendencies that warm during cold months (November–February) and cool during warm months (May–October),

311 thus reflecting the seasonal reversal of horizontal temperature gradients. Advection effects were most  
312 significant along the gulf–ocean boundary.

### 313 3.1.2 Mixed-layer heat budget for the seasonal cycle

314 To attribute the seasonal evolution mechanistically, the mixed-layer heat budget (Section 2.6) was applied and  
315 GAM and CS were compared (Figure 5). It was found that the air–sea heat-flux tendency  $(\partial T/\partial t)|_Q =$   
316  $Q_{net}/(\rho C_p h)$  dominates the seasonal cycle in both regions. The horizontal advection term  $(\partial T/\partial t)|_{adv} = -U \cdot$   
317  $\nabla T$  is generally an order of magnitude smaller, although it modulates the signal near the shelf edge. The  
318 summed tendency (flux + advection) [term](#) reproduces the observed monthly mixed-layer temperature tendency  
319 with a ~2-month lag (flux leads), which confirms that surface heat exchange sets the seasonal cycle, while  
320 advection acts in a secondary manner.

321 Seasonal extremes occur as follows: maximum warming rates from fluxes took place in June–July, and  
322 maximum cooling rates occurred in November–December, with stronger magnitudes recorded over GAM in  
323 winter and greater summer warming registered nearer to the CS. Advection is more energetic in GAM than in  
324 CS (notably during January–June and November–December), which resulted in warming during the cold season  
325 and cooling during the warm season. This is consistent with the sign of horizontal SST gradients. The residual  
326 (entrainment plus unresolved terms) is small at monthly scales, thus indicating that the flux and advection terms  
327 essentially achieve budget closure. It should be noted that the mixed-layer heat budget was applied solely to the  
328 seasonal cycle; longer-term variability is addressed in Sections 3.2–3.4 without a heat-budget decomposition.

### 329 3.2 Interannual variability, long-term trends and the 2011–2013 regime shift

330 Monthly linear trends of SST anomalies (Figure 6) reveal spatially coherent warming across the domain from  
331 2003 to 2022, with the largest magnitudes occurring in the transition and winter months. Peak grid-point trends  
332 occur in April and November, consistent with the domain-mean results, and were more pronounced along the  
333 shelf edge compared to offshore waters. Summer trends were weaker and spatially smoother, with local minima  
334 in June and July. By conducting stippling, ~~wethe authors~~ highlight grid cells [that are statistically significant at](#)  
335 [the 95% confidence level with  \$p < 0.05\$](#)  after adjusting for serial autocorrelation. Significant warming dominated  
336 most months, particularly from November to March and April.

337 Monthly SST anomalies (Figure 7a,c) show greater variability on the shelf (GAM) than offshore (CS), with  
338 standard deviations of 0.61°C and 0.41°C, respectively. Several cold winters marked the first half of the record  
339 (for example, 2004, 2009, 2011), which were more pronounced in GAM. An additional cold event in 2010 was  
340 evident in GAM but weak/absent in CS. In the second decade of study, warm winters predominated (for  
341 example, 2014, 2016, 2019, 2020), with stronger occurrences over GAM. Despite not every year conforming  
342 to the general trend, results demonstrate an overall evolution that is shifting from predominantly cool to  
343 predominantly warm conditions.

344 Seasonal means by year (Figure 7b,d) confirm that winter (January to March) drives most of the low-frequency  
345 change. Piecewise linear fits prior to and after 2011 indicate a winter cooling tendency during 2003–2011,  
346 followed by a marked winter warming during 2012–2022. Summer (July to September) warmed throughout the  
347 record, albeit with smaller slopes than winter in both regions. The black line in panels (b) and (d) of Figure 7  
348 shows the yearly linear trend, which is positive for both GAM and CS. In conjunction, these patterns indicate a  
349 step-like transition from 2011 to 2013 to a persistently warmer state, which is coherent across both shelf and  
350 offshore boxes. To formally assess whether the apparent transition toward a warmer state is statistically  
351 significant, we applied a changepoint test based on a two-phase regression with a common trend (XLW), which  
352 is designed to detect a step-like shift in the mean level while allowing for an underlying linear trend. The test  
353 was performed on the monthly SST anomaly series for the two representative subregions (GAM and CS; Fig.  
354 7a,c), scanning all admissible changepoint times and using the maximum F statistic (Fmax; see Reeves et al.,  
355 2007); significance was estimated via Monte Carlo simulation under the null with serial autocorrelation  
356 accounted for in the residual structure. The analysis identifies an optimal changepoint in December 2012 in  
357 both subregions, consistent with the step-like transition highlighted visually in Fig. 7b,d. The estimated mean-  
358 level increase after the changepoint is 0.67 °C for CS (Fmax = 53.45; 98% confidence) and 0.84 °C for GAM  
359 (Fmax = 35.75; 95% confidence). These results provide quantitative support that the late-2012 shift represents  
360 a statistically significant transition toward persistently warmer conditions in both shelf and offshore  
361 environments.

362 In summary, the shelf exhibits larger variance and a stronger wintertime response than the adjacent CS,  
363 consistent with Section 3.1 (shallower mixed layers and stronger air–sea coupling). This transition foreshadows  
364 the increase in marine heatwave activity (see below Section 3.3) and is consistent with the low-frequency  
365 modulation captured by the EOF analysis (Section 3.4).

### 366 **3.3 Marine heatwaves**

367 Spatially, the mean of event-wise maximum intensity ranges from ~1–2°C across the domain (Figure 8a), with  
368 a regional mean of  $1.3 \pm 0.2^\circ\text{C}$ . Intensities were systematically higher inside the gulf than offshore. Events in  
369 GAM tended to have higher absolute intensity, whereas the CS, which experienced lower background variance,  
370 more often reached higher MHW categories under the Hobday scheme. The total number of MHW days from  
371 2003 to 2022 exceeds 200 at every grid cell and surpasses 400 over most of the GAM (Figure 8b).

372 The year-by-year event calendars for the representative boxes (Figure 8c, d) show broadly similar annual  
373 frequencies in GAM and CS (typically 4–5 events  $\text{yr}^{-1}$ ), with a marked increase in frequency and intensity  
374 during the second decade. The most active period is 2019–2020, followed by 2015–2016, in both regions. The  
375 years 2004 and 2008 are the only ones in which no MHW was detected in either box. Accordingly, a key shelf–  
376 offshore contrast emerges: Events in GAM tended to be more intense, while more high-category events were  
377 registered in the CS; over the entire period, 73 events were recorded in GAM compared to 90 in CS. These  
378 patterns are consistent with the seasonal contrasts established in Section 3.1, i.e., shallow, strongly forced shelf

379 waters favour larger absolute temperature anomalies (higher intensity), while offshore, the background  
380 threshold and variance regime support more frequent escalation to higher categories.

### 381 **3.4 Modes of variability**

382 EOFs of monthly SST anomalies (2003–2022) indicate that the first two modes account for 93.7% of the total  
383 variance (EOF1: 87.5%, EOF2: 6.2%) and possess clear physical significance (Figure 9). EOF1 displays a  
384 monopole pattern with positive loadings across the domain, slightly enhanced toward the shelf edge and  
385 offshore. This mode represents coherent warming/cooling of the entire region. Its principal component (PC1)  
386 exhibits low-frequency variability with a pronounced minimum during the 2009–2011 period and positive  
387 excursions in the 2013–2016 and 2019–2020 periods. The 2-year low-pass PC1 highlights the step-like  
388 transition to a warmer state after the 2011–2013 period, consistent with Section 3.2 and with the increase in  
389 MHW activity (Section 3.3).

390 EOF2 is a dipole that opposes the shallow shelf (GAM/GG) to the adjacent CS, with larger amplitudes along  
391 the shelf break. This mode captures differential heating/cooling between coastal and oceanic waters, consistent  
392 with the seasonal mechanisms diagnosed in Section 3.1 (stronger air–sea coupling over the shelf and modulation  
393 by horizontal advection). PC2 fluctuates primarily at interannual timescales, exhibiting alternating  
394 positive/negative phases throughout the period of study, with no persistent trend identified. This indicates  
395 variability that redistributes anomalies between the shelf and offshore regions, rather than warming the entire  
396 region.

397 Overall, EOF1 reflects basin-wide anomalies that underpin the regime shift, whereas EOF2 explains spatial  
398 structure related to the shelf–offshore gradient. In Section 3.5, these modes are related to large-scale climate  
399 indices in order to assess likely drivers of the interannual–decadal variability.

### 400 **3.5 Climate drivers: EOF PCs vs large-scale indices**

401 ~~A relationship was established~~The authors of the present paper established a relationship between the leading  
402 SST modes and climate variability by comparing PC1/PC2 with standard indices (ENSO [MEI], WHWP, TNA  
403 and NAO, Section 2.4) and with domain-mean latent heat flux (LHF, ERA5). Interannual variability was  
404 isolated with a 2-year running-mean low-pass, and low-frequency variability with a 5-year running-mean low-  
405 pass (zero-lag correlations reported; significance assessed with effective degrees of freedom; Section 2.5).

406 At interannual scales (Figure 10a), PC1 co-varies with MEI ( $r \approx 0.4956$ ), WHWP ( $r \approx 0.58$ ), and especially with  
407 LHF ( $r \approx 0.734$ ), consistent with an air–sea heat-flux pathway linking climate modes to regional SST. At low  
408 frequencies (Figure 10c), PC1 closely tracks the NAO ( $r \approx 0.90$ ), consistent with the step-like warming observed  
409 after 2011–2013 (Section 3.2). The effective degrees of freedom ( $N^*$ ) and associated significance levels for all  
410 correlations (computed after low-pass filtering) are summarized in Table S3.

411 At interannual scales (Figure 10b), PC2 correlates with the TNA index ( $r \approx 0.53$ ), consistent with variability  
412 that redistributes anomalies between shelf and offshore rather than producing basin-wide warming. In  
413 conjunction, these results indicate that ENSO/WHWP modulates basin-wide anomalies (PC1) via latent heat

414 flux on interannual scales and through the NAO on low-frequency scales. Simultaneously, the shelf–offshore  
415 contrast (PC2) is tied to TNA-related variability. Physical mechanisms are discussed in Section 4.

## 416 **4. Discussion**

### 417 **4.1 Seasonal mechanisms and shelf–offshore contrast**

418 The mixed layer heat budget shows that air–sea heat exchange is the primary control on the seasonal evolution  
419 of surface temperature across the study area, with horizontal advection acting as a secondary modulator near  
420 the shelf break (Section 3.1). This result is entirely consistent with mixed layer theory and previous diagnostics  
421 with regards to tropical–subtropical shelves, where the net surface heat flux drives most of the seasonal  
422 tendency, while advection fine-tunes phasing and amplitude (Moisan and Niiler, 1998; de Boyer Montégut et  
423 al., 2004). In practice, net surface heat flux accounts for the marked winter cooling (November–March) and  
424 summer warming (April–September), whereas advection tends to warm during the cold season and then cool  
425 during the warm season, thus reflecting the seasonal reversal of horizontal SST gradients.

426 The contrast between GAM and the adjacent CS follows directly from this balance. Inside GAM, the mixed  
427 layer is shallower, so for any given flux, the temperature tendency ( $\propto Q_{\text{net}}/h$ ) is larger. This explains the faster  
428 winter cooling and the enhanced amplitude of the seasonal cycle within the gulf. Along the shelf edge, where  
429 SST gradients intensify, the advection term becomes more relevant, and it modulates peaks. Nevertheless, its  
430 magnitude remains smaller than the flux-driven tendency when monthly means are considered. The resulting  
431 picture, in which thermodynamics set the seasonal baseline and circulation provides fine-scale adjustment, is  
432 also consistent with the location and persistence of frontal structures aligned with the shelf break (Figure 2).  
433 These findings support hypothesis 1 of the present study and provide a mechanistic basis for the shelf–offshore  
434 SST contrast described for southern Cuba in previous work (Cerdeira Estrada et al., 2005; Caravaca et al., 2022;  
435 González De Zayas et al., 2022).

### 436 **4.2 Interannual–decadal drivers and 2011–2013 regime shift**

437 Superimposed on the seasonal cycle is a robust long-term warming, which is at its strongest during winter and  
438 transition months and is amplified over the shelf, in line with broader Caribbean tendencies (Avila-Alonso et  
439 al., 2020). The record exhibits a step-like transition between 2011 and 2013, from a relatively cool to a  
440 persistently warmer state, which is coherent throughout GAM and CS. Moreover, the modulation of the  
441 dominant climatic oscillations in the region (NAO, ENSO, WHWP) promotes the progressive accumulation of  
442 heat in the ocean surface layer and its transfer to subsurface levels, which is chiefly responsible for the long-  
443 term warming observed in the area. The EOF analysis clarifies the structure: EOF1 (87.5%) is a basin-wide  
444 mode with positive loadings across the domain and low-frequency fluctuations in PC1; EOF2 (6.2%) is a dipole  
445 which opposes shelf to offshore waters and primarily redistributes anomalies without an evident trend.

446 Relating these modes to large-scale variability (Figure 10) suggests two complementary pathways. At the  
447 interannual scales, PC1 co-varies with ENSO, the WHWP (Wang and Enfield, 2001, 2003; Enfield and Lee,  
448 2005), and most directly with LHF, which is consistent with trade wind and humidity anomalies that regulate  
449 evaporative cooling over the warm-pool region (Czaja et al., 2002; Wang et al., 2006). The lead-lag structure  
450 (indices leading SST by order of months) favours an air-sea coupling pathway rather than a purely oceanic  
451 origin. At low frequencies, PC1 correlates with the NAO (Hurrell, 1995), which suggests a broader Atlantic  
452 influence on winds and surface heat exchange and, in turn, is consistent with the timing of the 2011–2013  
453 transition. Conversely, PC2 correlates most closely with the TNA index (Enfield et al., 1999), in line with the  
454 differential heating between coastal and oceanic waters and the role of horizontal temperature gradients in  
455 setting advection (Section 3.1). Taken in conjunction, these results support hypotheses 2 and 3 of the present  
456 study: that basin-wide anomalies are largely atmospherically forced through heat flux pathways linked to  
457 ENSO/WHWP (interannual) and the NAO (low frequency), whereas the spatial structure within the region  
458 reflects regional thermodynamics and circulation.

#### 4.1 Seasonal and low-frequency drivers of SST variability

461 The seasonal evolution of SST in and around JRNP is primarily controlled, with net air-sea heat exchange  
462 setting both the sign and timing of the mixed-layer temperature tendency, and horizontal advection providing a  
463 secondary modulation near the shelf break. This behaviour is consistent with mixed-layer heat-budget theory,  
464 in which surface fluxes dominate the seasonal cycle and heat storage produces an intrinsic lag between forcing  
465 and response (De Boyer Montégut et al., 2004; Moisan and Niiler, 1998). The pronounced autumn–winter  
466 shelf–offshore contrast arises naturally from mixed-layer-depth differences: for comparable surface forcing, the  
467 shallow mixed layer inside the Gulf of Ana María yields larger temperature tendencies ( $\propto Q_{net}/h$ ), thereby  
468 producing faster cooling and stronger gradients than in the adjacent Caribbean Sea. The observed persistence  
469 of frontal structures aligned with the shelf edge supports a regime in which thermodynamic forcing establishes  
470 the large-scale seasonal baseline, while circulation refine the spatial structure. This interpretation is coherent  
471 with prior descriptions of SST variability around Cuba and the southern Cuban shelves, where shelf-ocean  
472 contrasts and regional exchange with the Caribbean Sea shape the spatial pattern of SST (González-De Zayas  
473 et al., 2022; Caravaca et al., 2022; Cerdeira-Estrada et al., 2005).

474 Superimposed on this seasonal baseline, the dominant interannual-decadal signal is captured by a coherent  
475 basin-wide mode (EOF1) that covaries with ENSO/WHWP and, most directly, with latent-heat-flux variability.  
476 This is physically consistent with established Caribbean air-sea coupling pathways, whereby ENSO-related  
477 atmospheric anomalies modulate trade winds and near-surface humidity over the warm-pool region, altering  
478 evaporative cooling and thus SST at interannual time scales (Wang et al., 2006; Enfield and Lee, 2005; Wang  
479 and Enfield, 2003; Czaja et al., 2002; Wang and Enfield, 2001). In this framework, latent heat flux acts as an  
480 efficient bridge between large-scale atmospheric variability and local SST anomalies: weaker trades and/or  
481 reduced air-sea humidity gradients reduce evaporation, thereby decreasing upward latent-heat loss and

482 favouring SST warming. The strong co-variability between PC1 and latent heat flux in our results is consistent  
483 with this pathway and supports an interpretation in which basin-wide SST anomalies are primarily  
484 atmospherically forced through surface turbulent fluxes.

485 This mechanistic perspective also provides a coherent explanation for the step-like transition toward a  
486 persistently warmer state during 2011–2013. The transition is spatially coherent across both, the shelf and  
487 offshore subregions and projects strongly onto EOF1/PC1, indicating that it reflects a regional scale forcing  
488 rather than a local artefact of subregion selection. At low frequencies, PC1 closely tracks the NAO, suggesting  
489 that Atlantic-scale atmospheric variability modulates the background state of surface forcing over the Intra-  
490 American Seas (Cook and Vizy, 2010; Wang et al., 2007; Hurrell, 1995). We therefore interpret the 2011–2013  
491 shift as the manifestation of a low-frequency change in atmospheric conditions, which is consistent with NAO-  
492 related variability, that favours reduced net surface heat loss (through changes in winds and turbulent fluxes),  
493 allowing heat to accumulate and the system to transition into a warmer mean state. This interpretation is further  
494 supported by the timing of the transition in the low-pass PC1 and its correspondence with the increase in MHW  
495 activity during the second decade of the record. While the present analysis cannot establish causality, the  
496 proposed mechanism is physically grounded and consistent with the documented influence of ENSO/WHWP  
497 and Atlantic variability on Caribbean air-sea coupling and evaporative cooling (Cook and Vizy, 2010; Wang et  
498 al., 2007; Wang et al., 2006; Enfield and Lee, 2005; Wang and Enfield, 2003; Czaja et al., 2002; Wang and  
499 Enfield, 2001; Hurrell, 1995).

500 Finally, the secondary mode (EOF2) helps interpret how large-scale variability translates into spatial structure  
501 at local scales. Its shelf–offshore dipole and relationship with the Tropical North Atlantic index indicate  
502 variability that redistributes anomalies between the semi-enclosed gulfs and the adjacent open Caribbean Sea  
503 rather than warming the entire region uniformly. Physically, such redistribution is consistent with differential  
504 mixed-layer coupling and with the role of horizontal gradients and shelf-break dynamics in shaping SST  
505 patterns. Importantly for JRNP, this multi-scale framework implies that MHW risk is conditioned by (i) the  
506 local thermodynamic sensitivity of shallow shelf waters to surface forcing and (ii) large-scale atmospheric  
507 variability that favours persistent warm anomalies, both of which are relevant for coral-reef thermal stress and  
508 associated ecological impacts (Cramer et al., 2020; Bruno et al., 2019; Van Hooidonk et al., 2015; Hughes et  
509 al., 2003). From an applied perspective, these results support monitoring surface heat fluxes and mixed-layer  
510 depth alongside large-scale indices (ENSO/WHWP and NAO) to provide a physically informed context for  
511 early-warning assessments in the JRNP under continued warming.

#### 512 **4.23 Marine heatwaves: intensity, category and recent escalation**

513 Marine heatwaves increased in frequency and intensity during the second decade, with 2019–2020 being the  
514 most active period, followed by 2015–2016 as the second most active. MHW detection and categorization  
515 follow Hobday et al. (2016, 2018). Relative to the local 90th-percentile threshold, the mean of event-wise  
516 maximum intensity is greater in GAM than offshore, while the total number of MHW days surpasses 400 across

517 large areas of the gulf. However, the higher category scales (for example, Severe) occur comparatively more  
518 often offshore (CS). This contrast is expected under the Hobday scheme, in which categories are defined by the  
519 magnitude of local threshold exceedance. Thus, regions with lower background variance can experience higher  
520 categories, even for more minor absolute anomalies. Physically, GAM develops larger °C anomalies due to  
521 shallow, strongly forced mixed layers, while CS more readily crosses category thresholds owing to tighter local  
522 variability.

523 The warmer background state after the 2011–2013 period effectively preconditions the region for MHW  
524 development, increasing both the likelihood and persistence of threshold exceedances. Mechanistically, this  
525 links back to Sections 3.1 and 3.5, whereby flux-dominated seasonality sets the baseline and phase, and large-  
526 scale atmospheric variability modulates the probability of sustained warm anomalies that seed or prolong  
527 events. These patterns echo broader reef-climate concerns in the Caribbean, where rising SSTs and  
528 compounding stressors have been associated with bleaching and ecological change (Hughes et al., 2003; Bruno  
529 et al., 2019; Cramer et al., 2020; van Hooidek et al., 2015), including at JRNP and neighbouring MPAs (Pina  
530 Amargós et al., 2011; Hernández-Fernández et al., 2011, 2016, 2019a; Gerhartz-Muro et al., 2018; Caballero-  
531 Aragón et al., 2020).

#### 532 **4.34 Limitations, assumptions and robustness**

533 Several methodological choices bound the interpretation. The budget is formulated for the bulk mixed layer  
534 and, as a consequence, ~~the authors of the present study~~ we used GLORYS12 mixed-layer temperature, depth  
535 and currents for internal consistency among terms, by computing all tendencies on a daily basis and averaging  
536 these to monthly values. MUR SST was reserved for descriptive and MHW analyses. At monthly scales, MLT  
537 and SST are well correlated; however, residual differences may persist at daily scales due to skin effects and  
538 diurnal warming.

539 ERA5 and GLORYS12 may exhibit coastal biases. Particularly, it was not possible to directly evaluate the  
540 realism of GLORYS12 currents in the gulfs or the adjacent CS because no in-situ velocity observations (for  
541 example, those undertaken by Acoustic Doppler Current Profiler moorings or high-frequency radars) were  
542 available for the study period. This is a non-trivial caveat: reproducing circulation in highly shallow, embayed  
543 shelves, such as the GAM and the GG, is notoriously challenging for global reanalyses. This is because the  
544 effective  $1/12^\circ$  (~8–9 km) resolution and required bathymetric smoothing under-resolve narrow channels, weak  
545 pressure-gradient flows and small eddies. Moreover, the abrupt depth changes along the shelf break and the  
546 roughness and enhanced bottom friction associated with coral-reef frameworks further challenge the  
547 representation by the model of nearshore dynamics. Accordingly, the advective term in the mixed-layer budget  
548 herein should be interpreted as a conservative lower bound, which captures sign and seasonality but, potentially,  
549 underestimates magnitudes close to the coast. Targeted in-situ current measurements and/or nested higher-  
550 resolution regional modelling would help refine the role of advection within the gulfs.

551 Trends and correlations account for serial autocorrelation through effective degrees of freedom. EOFs were  
552 analyzed from raw data as well as from data to which 2-year and 5-year low-pass filters were applied. While

553 filtering choices can shift correlation maxima to a certain degree, they do not alter the physical interpretation.  
554 The 1-km MUR record dictates the 20-year baseline (2003–2022) and is shorter than the canonical 30-year  
555 climatology. Thresholds and category counts may therefore be modestly sensitive to baseline choice; extending  
556 thresholds with longer-record products (for example, coarser-resolution SST) would represent a more thorough  
557 sensitivity check.  
558 Overall, such limitations do not alter the headline result: that surface heat flux dominates the seasonal cycle,  
559 that basin-wide anomalies are atmospherically forced, and that shelf–offshore contrasts arise from the interplay  
560 of mixed-layer depth and horizontal gradients.

#### 561 **4.45 Implications for JRNP and outlook**

562 Two immediate implications follow. First, the strong coupling between net heat flux and temperature, in  
563 conjunction with the typical ~two-month lag, suggest that simple seasonal outlooks based on forecasts of  
564 radiative and turbulent fluxes and mixed-layer depth could offer early warning of forthcoming warming or  
565 cooling within GAM. Second, routine tracking of ENSO/WHWP (interannual) and NAO (low-frequency)  
566 provides a large-scale context for risk assessment. Consequently, positive phases aligned with reduced latent-  
567 heat loss increase the likelihood of basin-wide warmth (PC1) and, consequently, of MHW occurrence and  
568 persistence.

569 Moving forward, the following aspects have the potential to directly contribute to improving knowledge and  
570 forecasting capacity in the region: (a) in-situ observation of currents and conductivity, temperature and depth  
571 (from moorings or gliders transects) within JRNP and across the shelf break; (b) extended MHW climatologies,  
572 for example, by deriving thresholds from longer-record SST products, while retaining MUR for spatial detail;  
573 (c) targeted analyses of regional circulation features, such as shelf-break jets or eddy interactions, that may  
574 enhance advection during transition seasons at the local level; and (d) a practical next step is to implement a  
575 regional, high-resolution ocean model (for example, CROCO) nested in GLORYS12/ERA5 and tailored to the  
576 JRNP–GAM–GG system. A horizontal resolution of ~1 km or finer (with tidal forcing, realistic bathymetry/reef  
577 roughness and bulk fluxes) would enhance efforts to resolve shelf-break jets, gulf exchanges and frontal  
578 dynamics that are under-represented in global reanalyses. Such steps would not only consolidate the  
579 mechanistic framework presented herein, but also help to translate it into operational guidance for conservation  
580 and management within the national park.

## 581 **5. Conclusions**

582 The present study has quantified seasonal-to-decadal variability of sea-surface temperature (SST) in and around  
583 the Jardines de la Reina National Park (JRNP), with the primary objective to identify the mechanisms and  
584 climate drivers that shape this variability, using daily 1-km MUR SST (2003–2022), ERA5 surface fluxes and  
585 GLORYS12 mixed-layer fields.

586 A mixed-layer heat budget shows that net surface heat flux sets the seasonal evolution of SST, with horizontal  
587 advection providing a smaller modulation near the shelf break; a characteristic ~2-month lead of flux over  
588 temperature is consistent with mixed-layer heat storage and explains the enhanced winter cooling and stronger  
589 thermal gradients along the shelf edge. A clear shelf–offshore contrast emerges: the shallow gulfs (GAM/GG)  
590 markedly differ from the adjacent Caribbean Sea (CS) in autumn–winter (November–March), whereas  
591 conditions during spring–summer are comparatively homogeneous. This reflects shallower mixed layers and  
592 greater flux sensitivity inside the gulfs, with advection adding local modulation. Superimposed on this baseline  
593 is a warming trend of  $\sim 0.28^{\circ}\text{C}/\text{decade}^{-1}$  (2003–2022), which is strongest in winter and transition months, with  
594 monthly maxima around April ( $\sim 0.48^{\circ}\text{C}/\text{decade}^{-1}$ ) and November ( $\sim 0.35^{\circ}\text{C}/\text{decade}^{-1}$ ), and a step-like transition  
595 in 2011–2013 towards a persistently warmer state. The warming trend is predominantly driven by the phase  
596 shift of the NAO, since the study period begins in a negative phase and ends in a positive phase. In addition,  
597 the interannual to decadal modulation of other dominant climatic oscillations in the region (ENSO, WHWP),  
598 in conjunction with latent heat fluxes, favours the progressive accumulation of heat in the ocean surface layer.  
599 Marine heatwaves intensified during the second decade (with the 2019–2020 period the most active, followed  
600 by 2015–2016). Mean event-wise maximum intensity is higher within GAM, whereas upper categories occur  
601 relatively more often offshore, consistent with lower background variance in the area, while total MHW days  
602 exceed 200 across the domain and 400 over much of the gulf. EOFs separate a basin-wide mode (EOF1, 87.5%),  
603 co-varying interannually with ENSO/WHWP and latent-heat flux and at low frequencies with the NAO, from  
604 a shelf–offshore dipole (EOF2, 6.2%) linked most clearly to TNA. This indicates atmospheric forcing of basin-  
605 wide anomalies with regional thermodynamics and advection setting spatial structure.  
606 Practically, seasonal outlooks based on forecasts of net heat flux and mixed-layer depth, in addition to routine  
607 monitoring of ENSO/WHWP and NAO, can help to inform MHW risk in relation to JRNP. Indeed, a regional  
608 high-resolution ocean model (for example, ROMS/CROCO at  $\sim 1$  km or finer), combined with targeted in-situ  
609 observations, would further improve prediction and attribution. In conjunction, the results of the present  
610 research provide a physically grounded baseline for anticipating future thermal stress and for guiding  
611 conservation and management efforts within JRNP in response to continued climate warming.  
612

613 **Code and data availability:**

614 The data supporting the findings of this study are openly available from public repositories. Sea surface  
615 temperature data from the MUR dataset can be accessed at the JPL Physical Oceanography Distributed Active  
616 Archive Center (PODAAC, <https://podaac.jpl.nasa.gov>). The GLORYS12 ocean reanalysis data used are  
617 available through the Copernicus Marine Environment Monitoring Service (<https://marine.copernicus.eu>).  
618 ERA5 reanalysis data can be obtained from the European Centre for Medium-Range Weather Forecasts  
619 Climate Data Store (<https://cds.climate.copernicus.eu>). All processed data and analysis scripts are referenced  
620 in the manuscript and are available upon reasonable request.

621 **Author contribution:**

622 MC conceived the original idea, performed data analysis and image visualization and was responsible for  
623 writing the manuscript. OP co-conceived the original idea, helped interpret the results and provided key input  
624 in discussions and further writing. He also served as supervisor. AM contributed with the preparation of the  
625 original idea and conducted a review of the results and discussions. He was co-supervisor. IPS undertook data  
626 analysis and result interpretation and played a key role in discussions pertaining to heat balance. DC  
627 performed analysis of the MHWs and heat balance and supported the writing and interpretation of the results  
628 and discussions. DB endorsed the analysis and interpretation of SST trends and assisted in reviewing the  
629 manuscript. LC provided support with image processing using the geographic information system (QGis).

630 **Competing interests:**

631 The authors do not declare ~~no~~ conflicts of interest.

632 **Acknowledgements:**

633 ~~We~~The authors wish to thank the reviewers for their comments, which contributed significantly to the  
634 improvement of the quality of the manuscript. They are grateful to all collaborators and institutions that  
635 contributed to the preparation of the present manuscript. They also acknowledge the financial support of  
636 various national and international funding agencies. We used Grammarly, DeepL, and MS Word corrector  
637 during the writing of the manuscript.

638 Data access notes: MEI.v2 and the WHWP/TNA indices were retrieved from the NOAA PSL portals; the  
639 NAO index was retrieved from NOAA CPC (accessed in 2024–2025; URLs listed in the Data Availability  
640 statement).

641 **Financial support:**

642 This research was supported by the National Agency for Research and Development of Chile (ANID), Grant  
643 21211088 for the PhD in Oceanography at the Universidad de Concepción and partially funded by the  
644 Chilean Millennium Institute of Oceanography (IMO) (grant IC-120019) and the postgraduate department of

645 the Universidad de Concepción. Iván Pérez-Santos was funded by COPAS COASTAL (ANID FB210021)  
646 and FONDECYT 1251038. OP thanks support from FONDECYT 1241203.

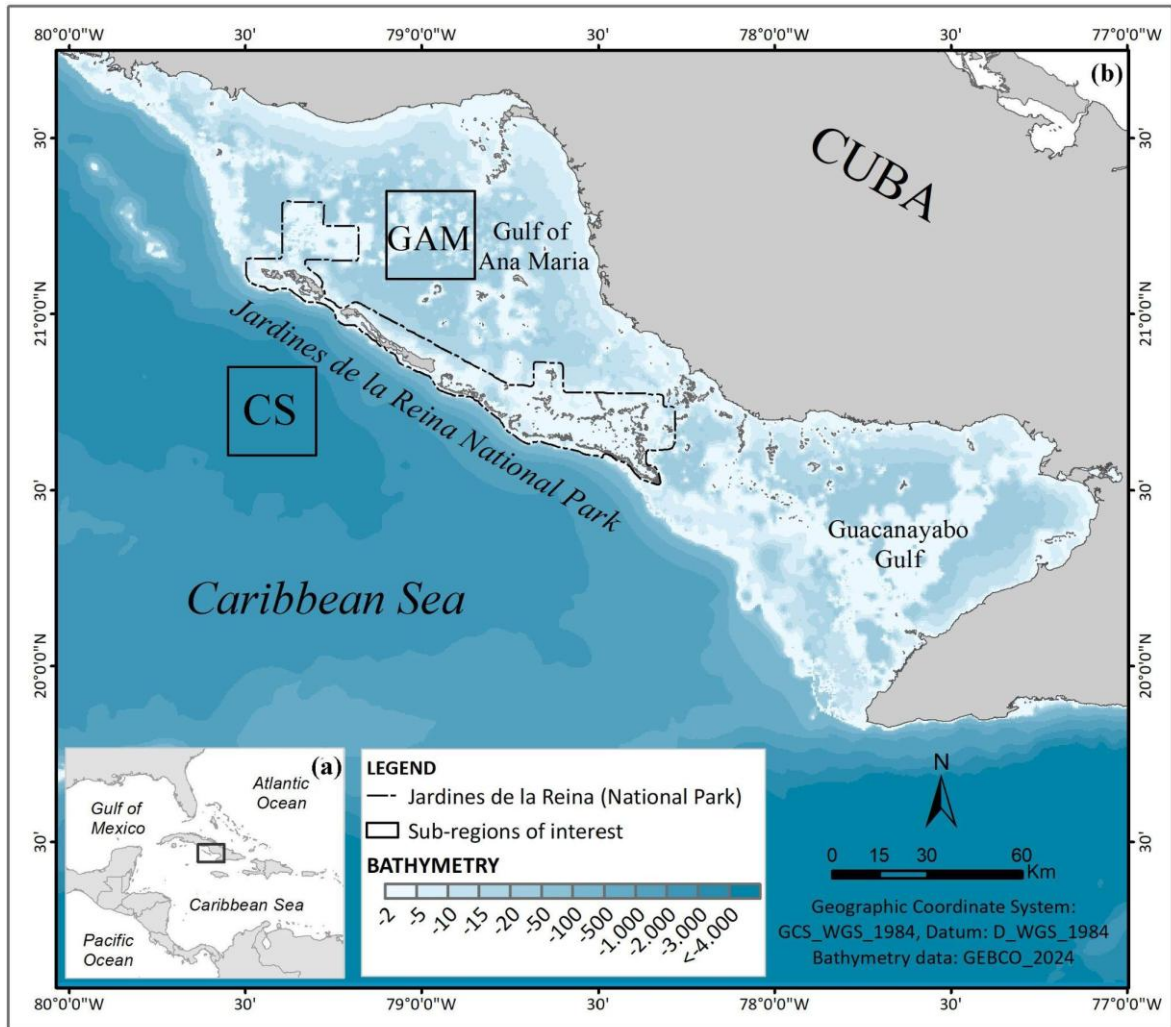
647 **References**

- 648 Appeldoorn, R. S. and Lindeman, K. C.: A Caribbean-wide survey of marine reserves: spatial coverage and  
649 attributes of effectiveness, *Gulf and Caribbean Research*, 14, 139–154, 2003.
- 650 Arriaza, L., Simanca, J., Rodas, R., Lorenzo, S., Hernández, M., Linares, E. O., Milian, D., and Romero, P.:  
651 Corrientes marinas estimadas en la plataforma suroriental cubana, *Serie Oceanológica*, 4, 1-10, 2008.
- 652 Avila-Alonso, D., Baetens, J. M., Cardenas, R., and De Baets, B.: Spatio-temporal variability of oceanographic  
653 conditions in the Exclusive Economic Zone of Cuba, *Journal of Marine Systems*, 212, 103416, 2020.
- 654 Barnston, A. G. and Livezey, R. E.: Classification, seasonality and persistence of low-frequency atmospheric  
655 circulation patterns, *Monthly Weather Review*, 115, 1083–1126, 1987.
- 656 Bruno, J. F., Côté, I. M., and Toth, L. T.: Climate change, coral loss, and the curious case of the parrotfish  
657 paradigm: why don't marine protected areas improve reef resilience?, *Annual Review of Marine Science*, 11,  
658 307–334, 2019.
- 659 Caballero-Aragón, H., Perera-Valderrama, S., Rey-Villiers, N., González-Méndez, J., and Armenteros, M.:  
660 Population status of *Acropora palmata* (Lamarck, 1816) in Cuban coral reefs, *Regional Studies in Marine  
661 Science*, 34, 101029, <https://doi.org/10.1016/j.rsma.2019.101029>, 2020.
- 662 Caravaca, A. M., Torres, L. C., and Alfonso, L. V.: Sea Surface Temperature Trends in the Southern Cuban  
663 Shelves for the Period 1982–2018, *Cham*, 81-90, 2022.
- 664 Cerdeira-Estrada, S., Müller-Karger, F. E., and Gallegos-García, A.: Variability of the sea surface temperature  
665 around Cuba, *Gulf of Mexico Science*, 23, 2, 2005.
- 666 Chang, Y.-L. and Oey, L.-Y.: Coupled response of the trade wind, SST gradient, and SST in the Caribbean Sea,  
667 and the potential impact on Loop Current's interannual variability, *Journal of Physical Oceanography*, 43,  
668 1325–1344, 2013.
- 669 Chen, H. C., Jin, F.-F., and Jiang, L.: The phase-locking of tropical North Atlantic and the contribution of  
670 ENSO, *Geophysical Research Letters*, 48, e2021GL095610, 2021.
- 671 Chen, W. Y. and Van den Dool, H.: Sensitivity of teleconnection patterns to the sign of their primary action  
672 center, *Monthly Weather Review*, 131, 2885–2899, 2003.
- 673 Chin, T. M., Vazquez-Cuervo, J., and Armstrong, E. M.: A multi-scale high-resolution analysis of global sea  
674 surface temperature, *Remote Sensing of Environment*, 200, 154–169, <https://doi.org/10.1016/j.rse.2017.07.029>,  
675 2017.
- 676 Chollett, I., Mumby, P. J., Müller-Karger, F. E., and Hu, C.: Physical environments of the Caribbean Sea,  
677 *Limnology and Oceanography*, 57, 1233–1244, 2012.
- 678 Cook, K. and Vizy, E.: Hydrodynamics of the Caribbean low-level jet and its relationship to precipitation,  
679 *Journal of Climate*, 23, 1477–1494, 2010.
- 680 Cramer, K. L., Jackson, J. B. C., Donovan, M. K., Greenstein, B. J., Korpanty, C. A., Cook, G. M., and Pandolfi,  
681 J. M.: Widespread loss of Caribbean acroporid corals was underway before coral bleaching and disease  
682 outbreaks, *Science Advances*, 6, eaax9395, <https://doi.org/10.1126/sciadv.aax9395>, 2020.
- 683 Czaja, A., Van der Vaart, P., and Marshall, J.: A diagnostic study of the role of remote forcing in tropical  
684 Atlantic variability, *Journal of Climate*, 15, 3280–3290, 2002.

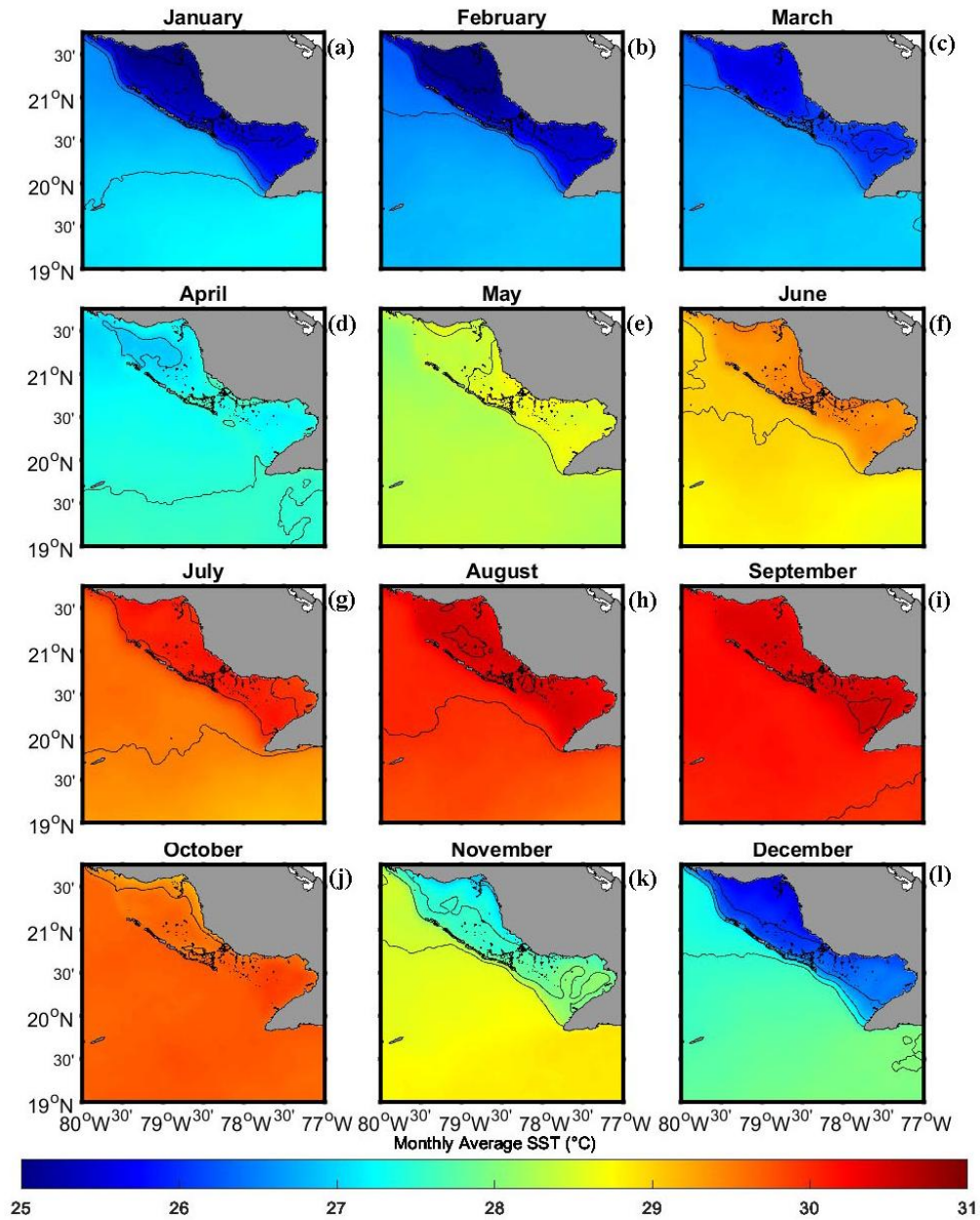
- 685 de Boyer Montégut, C., Madec, G., Fischer, A. S., Lazar, A., and Iudicone, D.: Mixed layer depth over the  
686 global ocean: An examination of profile data and a profile-based climatology, *Journal of Geophysical Research:*  
687 *Oceans*, 109, 2004.
- 688 Emilsson, I. and Tápanes, J. J.: Contribución a la hidrología de la plataforma sur de Cuba, *Serie Oceanológica*,  
689 9, 1971.
- 690 Enfield, D. B. and Lee, S.-K.: The heat balance of the Western Hemisphere warm pool, *Journal of Climate*, 18,  
691 2662–2681, 2005.
- 692 Enfield, D. B., Mestas-Núñez, A. M., Mayer, D. A., and Cid-Serrano, L.: How ubiquitous is the dipole  
693 relationship in tropical Atlantic sea surface temperatures?, *Journal of Geophysical Research: Oceans*, 104,  
694 7841–7848, 1999.
- 695 Fernández, L. H. and López, C. B.: Condición de la población de ACROPORA PALMATA LAMARCK, 1816  
696 en arrecifes del Parque Nacional Jardines de la Reina, Cuba, *Revista de Investigaciones Marinas*, 37, 2017.
- 697 Gerhartz-Muro, J. L., Kritzer, J. P., Gerhartz-Abraham, A., Miller, V., Pina-Amargós, F., and Whittle, D.: An  
698 evaluation of the framework for national marine environmental policies in Cuba, *Bulletin of Marine Science*,  
699 94, 443–459, 2018.
- 700 González-De Zayas, R., Pupo, F. M., González, J. A. L., and Hernández-Fernández, L.: Temporal behavior of  
701 air and sea surface temperature in a marine protected area of Cuba: the Jardines de la Reina National Park,  
702 *Holos Environment*, 22, 46–64, 2022.
- 703 Graham, N. A. J., Jennings, S., MacNeil, M. A., Mouillot, D., and Wilson, S. K.: Predicting climate-driven  
704 regime shifts versus rebound potential in coral reefs, *Nature*, 518, 94–97, 2015.
- 705 Hernández-Fernández, L., González de Zayas, R., Olivera, Y. M., Pina Amargós, F., Bustamante López, C.,  
706 Dulce Sotolongo, L. B., Bretos, F., Figueredo Martín, T., Lladó Cabrera, D., and Salmón Moret, F.: Distribution  
707 and status of living colonies of *Acropora* spp. in the reef crests of a protected marine area of the Caribbean  
708 (Jardines de la Reina National Park, Cuba), *PeerJ*, 7, e6470, 2019.
- 709 Hernández-Fernández, L., Guimaraes Bermejo, M., Arias Barreto, R., and Clero Alonso, L.: Composición de  
710 las comunidades de octocorales y corales pétreos y la incidencia del blanqueamiento del 2005 en Jardines de la  
711 Reina, Cuba, *Journal of Marine and Coastal Sciences*, 3, 77–90, 2011.
- 712 Hobday, A. J., Alexander, L. V., Perkins, S. E., Smale, D. A., Straub, S. C., Oliver, E. C. J., Benthuisen, J. A.,  
713 Burrows, M. T., Donat, M. G., and Feng, M.: A hierarchical approach to defining marine heatwaves, *Progress*  
714 *in Oceanography*, 141, 227–238, 2016.
- 715 Hobday, A. J., Oliver, E. C. J., Sen Gupta, A., Thomas, L., and Benthuisen, J. A.: Categorizing and naming  
716 marine heatwaves, *Oceanography*, 31(2), 162–173, 2018.
- 717 Hughes, T. P., Baird, A. H., Bellwood, D. R., Card, M., Connolly, S. R., Folke, C., Grosberg, R., Hoegh-  
718 Guldberg, O., Jackson, J. B. C., and Kleypas, J.: Climate change, human impacts, and the resilience of coral  
719 reefs, *Science*, 301, 929–933, 2003.
- 720 Hurrell, J. W.: Decadal trends in the North Atlantic Oscillation: regional temperatures and precipitation,  
721 *Science*, 269, 676–679, 1995.
- 722 Jackson, J., Donovan, M., Cramer, K., and Lam, V.: Status and trends of Caribbean coral reefs: 1970–2012,  
723 *Global Coral Reef Monitoring Network (GCRMN)*, IUCN, Gland, Switzerland, 2014.

- 724 Kumagai, N. H. and Yamano, H.: High-resolution modelling of thermal thresholds and environmental  
725 influences on coral bleaching for local and regional reef management, *PeerJ*, 6, e4382, 2018.
- 726 Linton, D., Smith, R., Alcolado, P., Hanson, C., Edwards, P., Estrada, R., Fisher, T., Fernandez, R. G., Gerald  
727 F., and McCoy, C.: 15. Status of coral reefs in the northern Caribbean and Atlantic node of the GCRMN, in:  
728 Status of Coral Reefs of the World: 2002, Australian Institute of Marine Science; Global Coral Reef Monitoring  
729 Network, 277-302, 2002.
- 730 Lotze, H. K., Lenihan, H. S., Bourque, B. J., Bradbury, R. H., Cooke, R. G., Kay, M. C., Kidwell, S. M., Kirby,  
731 M. X., Peterson, C. H., and Jackson, J. B. C.: Depletion, degradation, and recovery potential of estuaries and  
732 coastal seas, *Science*, 312, 1806–1809, 2006.
- 733 Moisan, J. R. and Niiler, P. P.: The seasonal heat budget of the North Pacific: net heat flux and heat storage  
734 rates (1950–1990), *Journal of Physical Oceanography*, 28, 401–421, 1998.
- 735 Mumby, P. J., Flower, J., Chollett, I., Box, S. J., Bozec, Y.-M., Fitzsimmons, C., Forster, J., Gill, D., Griffith-  
736 Mumby, R., and Oxenford, H. A.: Towards reef resilience and sustainable livelihoods: a handbook for  
737 Caribbean coral reef managers, University of Exeter, Exeter, 2014.
- 738 Pérez-Santos, I., Schneider, W., Sobarzo, M., Montoya-Sánchez, R., Valle-Levinson, A., and Garcés-Vargas,  
739 J.: Surface wind variability and its implications for the Yucatán Basin–Caribbean Sea dynamics, *Journal of*  
740 *Geophysical Research: Oceans*, 115, C10052, 2010.
- 741 Skerrett, F., Adelson, A., and Collin, R.: Performance of high-resolution MUR satellite sea surface temperature  
742 data as a proxy for near-surface in situ temperatures on neotropical reefs, *Latin American Journal of Aquatic*  
743 *Research*, 52, 270–288, 2024.
- 744 Thomson, R. E. and Emery, W. J.: *Data Analysis Methods in Physical Oceanography*, 4th edn., Elsevier,  
745 Amsterdam, 2024.
- 746 Van den Dool, H., Saha, S., and Johansson, A.: Empirical orthogonal teleconnections, *Journal of Climate*, 13,  
747 1421–1435, 2000.
- 748 van Hooidek, R., Maynard, J. A., Liu, Y., and Lee, S. K.: Downscaled projections of Caribbean coral bleaching  
749 that can inform conservation planning, *Global Change Biology*, 21, 3389–3401, 2015.
- 750 Venegas, R. M., Acevedo, J., and Treml, E. A.: Three decades of ocean warming impacts on marine ecosystems:  
751 a review and perspective, *Deep-Sea Research Part II: Topical Studies in Oceanography*, 212, 105318, 2023.
- 752 Waliser, D. and Jiang, X.: Tropical meteorology and climate: Intertropical Convergence Zone, *Encyclopedia of*  
753 *atmospheric sciences*, 6, Elsevier, 121-131, 2015.
- 754 Wang, C. and Enfield, D. B.: The tropical Western Hemisphere warm pool, *Geophysical Research Letters*, 28,  
755 1635–1638, 2001.
- 756 Wang, C. and Enfield, D. B.: A further study of the tropical Western Hemisphere warm pool, *Journal of Climate*,  
757 16, 1476–1493, 2003.
- 758 Wang, C., Enfield, D. B., Lee, S.-K., and Landsea, C. W.: Influences of the Atlantic warm pool on Western  
759 Hemisphere summer rainfall and Atlantic hurricanes, *Journal of Climate*, 19, 3011–3028, 2006.
- 760 Wang, C., Lee, S.-K., and Enfield, D. B.: Impact of the Atlantic warm pool on the summer climate of the  
761 Western Hemisphere, *Journal of Climate*, 20, 5021–5040, 2007.

- 762 Wolter, K.: Monitoring ENSO in COADS with a seasonally adjusted principal component index, in:  
763 Proceedings of the 17th Climate Diagnostics Workshop, 1993.
- 764 Zhang, T., Hoell, A., Perlwitz, J., Eischeid, J., Murray, D., Hoerling, M., and Hamill, T. M.: Towards  
765 probabilistic multivariate ENSO monitoring, *Geophysical Research Letters*, 46, 10532–10540, 2019.
- 766



768  
 769 **Figure 1.** Study area and sub-regions. (a) Regional setting: Cuba in the Caribbean Sea (CS), with the study  
 770 domain indicated by the black rectangle. (b) Southeastern Cuban shelf showing the Jardines de la Reina National  
 771 Park (black polygon) and neighbouring gulfs: Gulf of Ana María (GAM) and Gulf of Guacanayabo (GG). Black  
 772 boxes mark the two analysis sub-regions: GAM (shelf) and CS (oceanic). Colour shading shows bathymetry  
 773 (m) from GEBCO\_2024.  
 774



776

777

778

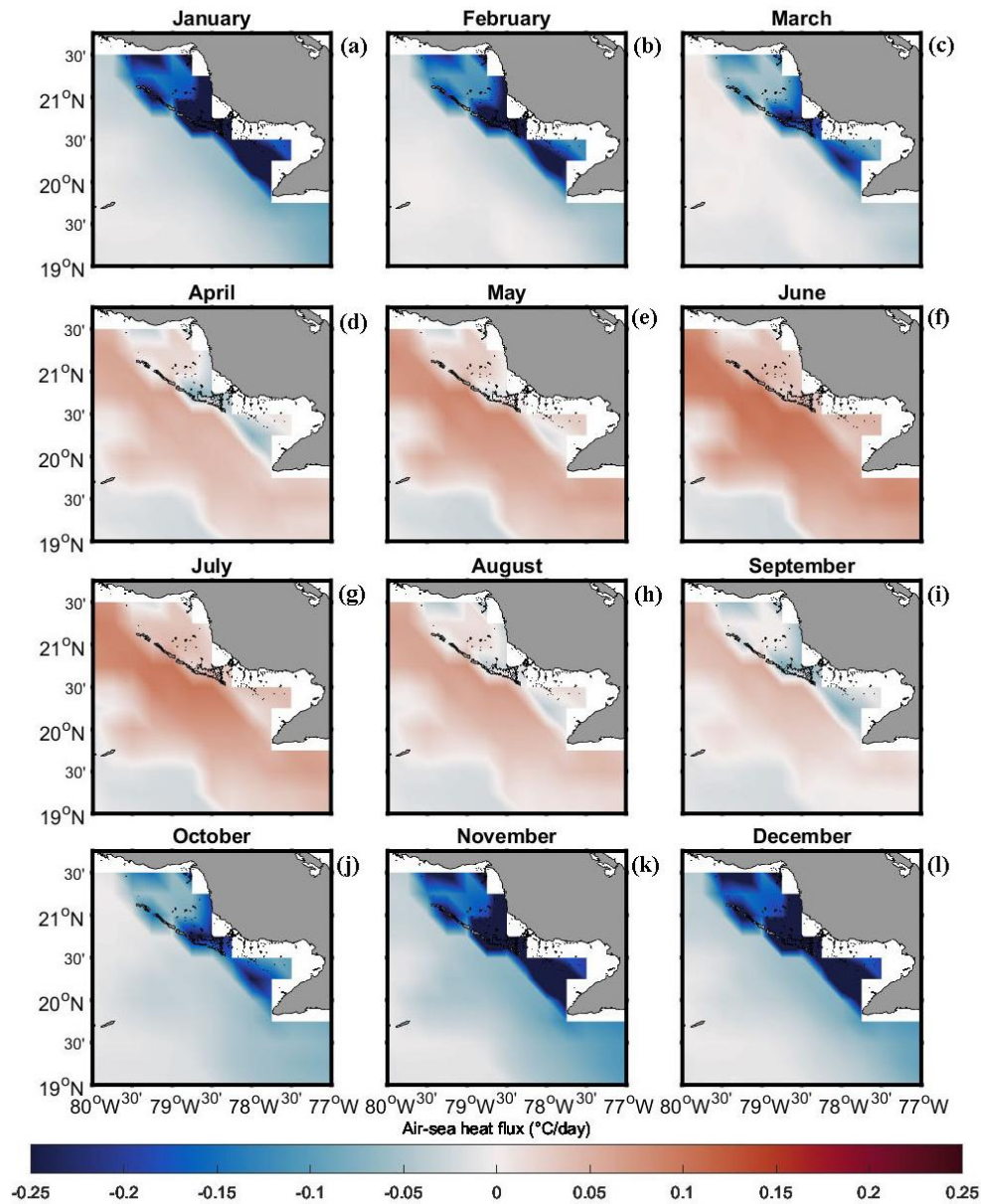
779

780

781

782

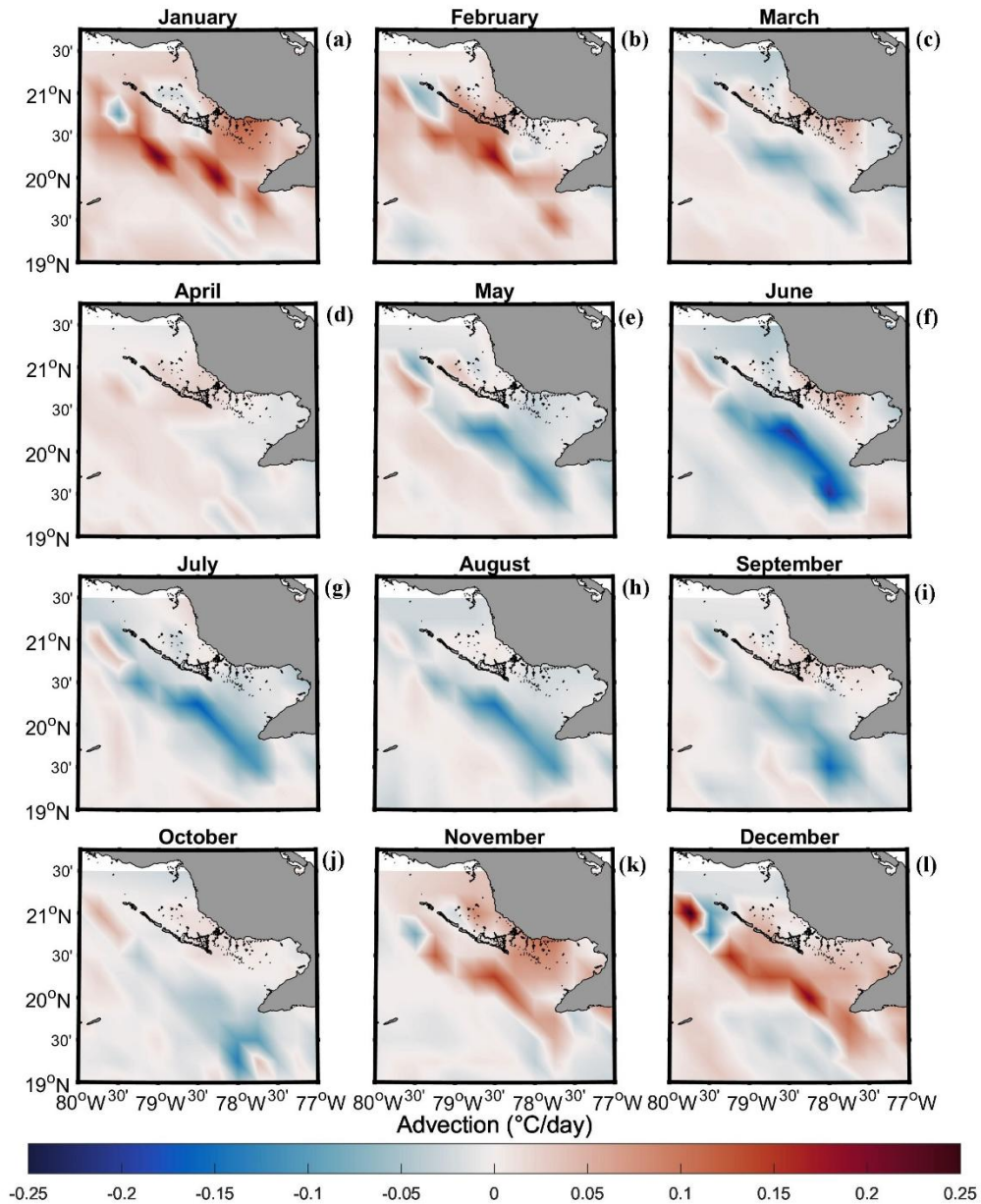
**Figure 2.** Monthly SST climatology (based on period 2003–2022). Panels (a–l) show monthly mean sea-surface temperature (°C) from January to December. Black contours mark SST fronts identified, where local horizontal SST differences are  $\geq 0.5$  °C. Seasonal groupings are: (a–c) boreal winter (JFM), (d–f) spring (AMJ), (g–i) summer (JAS), and (j–l) autumn (OND). The colour bar indicates monthly mean SST (°C); land is masked in grey.



784

785 **Figure 3.** Monthly air-sea heat-flux tendency [term\(2003–2022\)](#). Panels (a–l) show the monthly mean mixed-  
 786 layer heating rate due to net air-sea heat exchange, expressed as  $^{\circ}\text{C day}^{-1}$  and computed as  $(\partial T/\partial t)|_Q =$   
 787  $Q_{net}/(\rho C_p h)$ . Positive (red) warms the ocean; negative (blue) cools the ocean. Months run January–December;  
 788 seasonal groupings are (a–c) boreal winter (JFM), (d–f) spring (AMJ), (g–i) summer (JAS), and (j–l) autumn  
 789 (OND). Flux components are from ERA5, mixed-layer depth  $h$  from GLORYS12 [all variables are for the period](#)  
 790 [2003–2022](#); land is masked in grey.

791



793

794

795

796

797

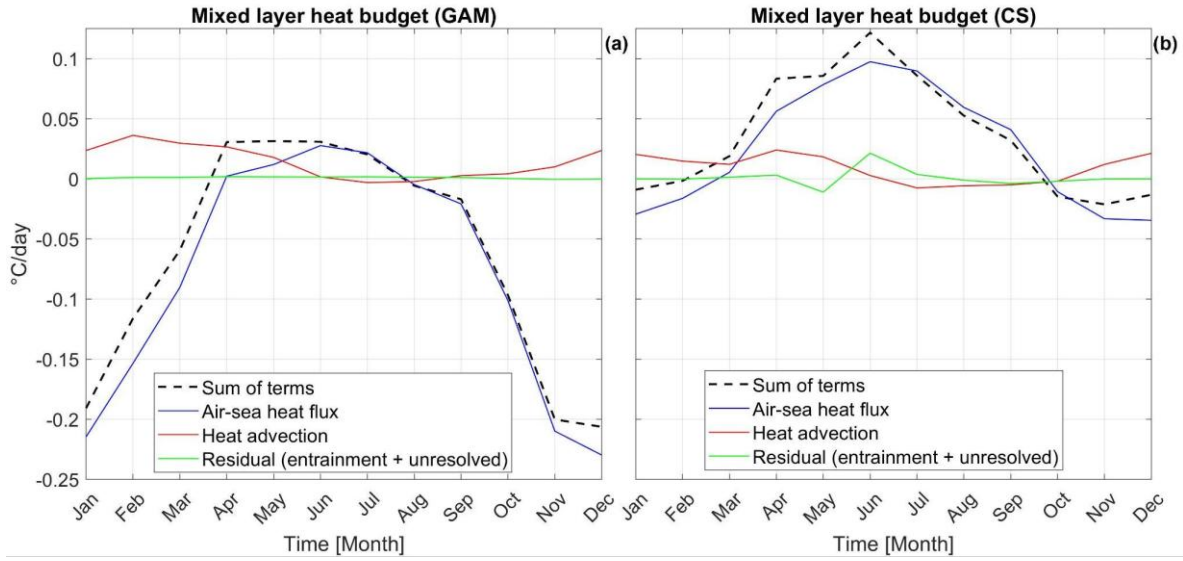
798

799

800

**Figure 4.** Monthly horizontal heat-advection tendency [term\(2003–2022\)](#). Panels (a–l) show the monthly mean mixed-layer temperature tendency due to horizontal advection, expressed as  $^{\circ}\text{C day}^{-1}$  and computed as  $(\partial T/\partial t)|_{adv} = -U \cdot \nabla T$ . Positive (red) warms the mixed layer; negative (blue) cools it. Currents and temperature gradients are from GLORYS12 (ML-averaged currents and mixed-layer temperature) [all variables are for the period 2003–2022](#); land is masked in grey.

801

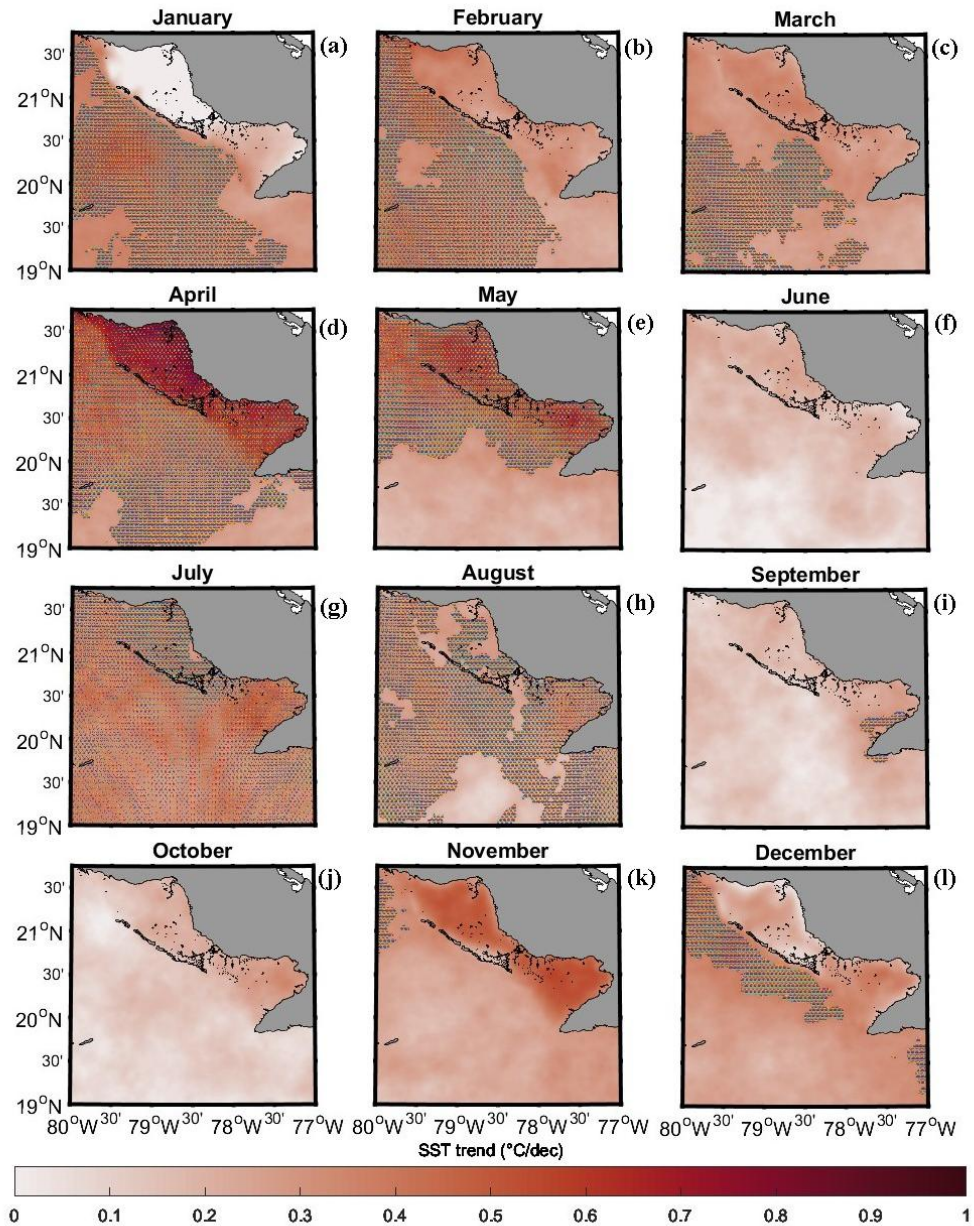


802

803 **Figure 5.** Seasonal mixed-layer heat budget (2003–2022). Monthly climatologies of mixed-layer temperature  
 804 tendencies ( $^{\circ}\text{C day}^{-1}$ ) for (a) GAM and (b) CS. Blue line: air–sea heat-flux tendency  $(\partial T/\partial t)|_Q =$   
 805  $Q_{net}/(\rho C_p h)$ . Red line: horizontal advection  $(\partial T/\partial t)|_{adv} = -U \cdot \nabla T$ . Dashed black line: sum of resolved  
 806 terms (flux + advection). Green line: residual (entrainment + unresolved processes), computed as the observed  
 807 mixed-layer temperature tendency minus the sum of resolved terms. Positive values warm the mixed layer;  
 808 negative values cool it. All terms were computed from daily fields and averaged to monthly means; see Section  
 809 2.6 for data sources and sign conventions.

810

811

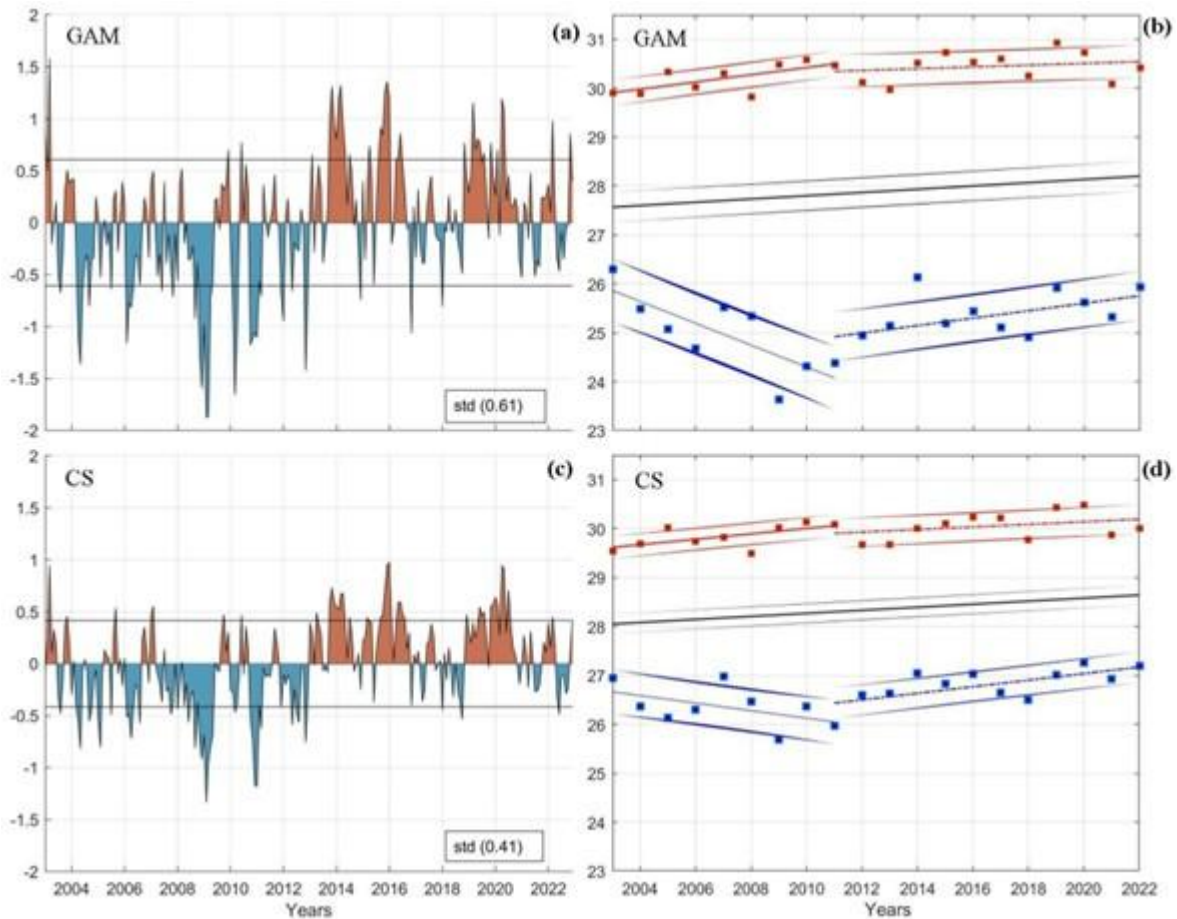


813

814

**Figure 6.** Monthly SST trends (2003–2022). Linear trends of monthly SST anomalies ( $^{\circ}\text{C decade}^{-1}$ ) for  
 815 January–December (panels a–l). Trends are estimated by ordinary least squares applied to monthly anomalies  
 816 at each grid point. Stippling indicates grid cells that are significant at the 95% level (two-sided t-test), using  
 817 effective degrees of freedom to account for autocorrelation. Warming intensifies in winter and transition  
 818 months, with maxima in April and November; land is masked in grey.

819



821

822

823

824

825

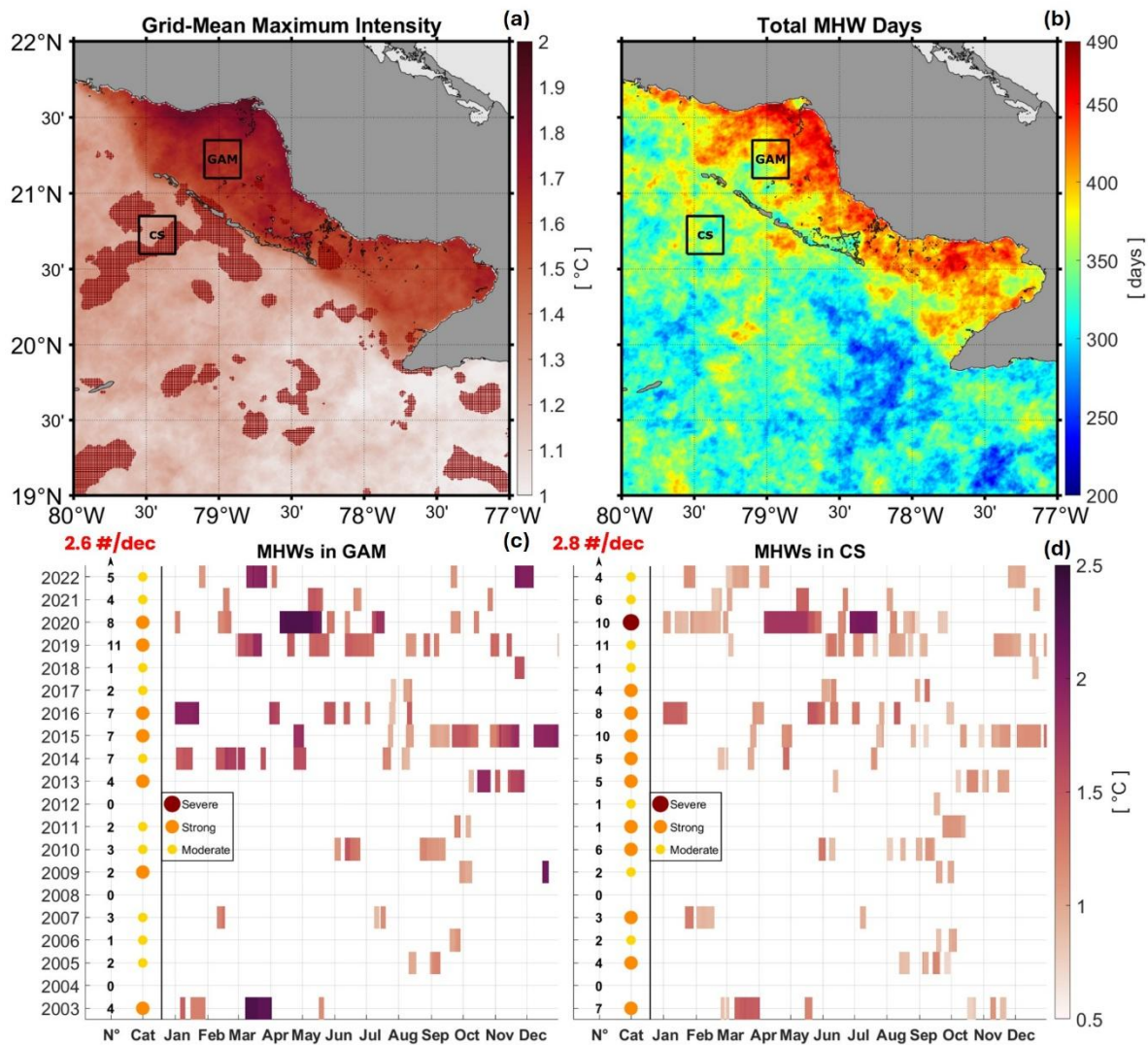
826

827

828

829

**Figure 7.** (a,c) Monthly SST anomalies ( $^{\circ}\text{C}$ ) for the Gulf of Ana María (GAM) and the Caribbean Sea (CS), respectively, 2003–2022. Thin horizontal black lines indicate  $\pm 1$  standard deviation over the full period (value shown in each panel). (b,d) Yearly seasonal means for summer (July–August–September; red squares) and winter (January–February–March; blue squares) in GAM and CS, respectively. Black lines show linear trends of the annual means. Coloured lines show piecewise linear fits to the seasonal means prior to (2003–2011) and after (2012–2022) the 2011 transition. All series represent area averages over the GAM and CS boxes shown in Figures 1a and 1b.



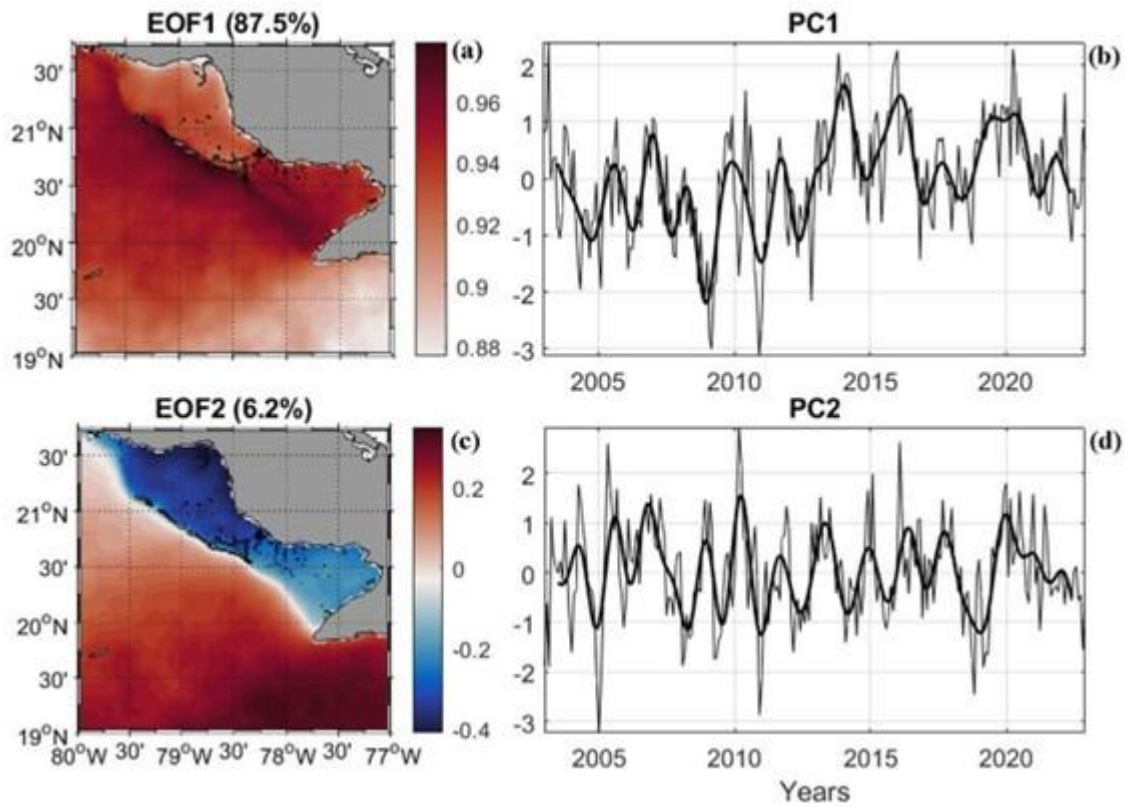
831

832

**Figure 8.** Marine heatwave (MHW) characteristics between 2003–2022. (a) Mean of event-wise maximum intensity (°C) at each grid point. Grid cells that experienced Severe category events at least once are shaded (reddish shading). (b) Total MHW days per grid point accumulated from 2003 to 2022. Black boxes mark the GAM and CS sub-regions. (c–d) Event calendars for GAM and CS, respectively: coloured rectangles denote individual events by month, with darker shading indicating increased intensity (°C). Left-hand columns indicate, for each year, the number of events (N°) and the maximum category reached (circle colour: Moderate/Strong/Severe). At the top left of c-d, the trend in event frequency is shown as the number of events per decade (#/dec).

840

841



842

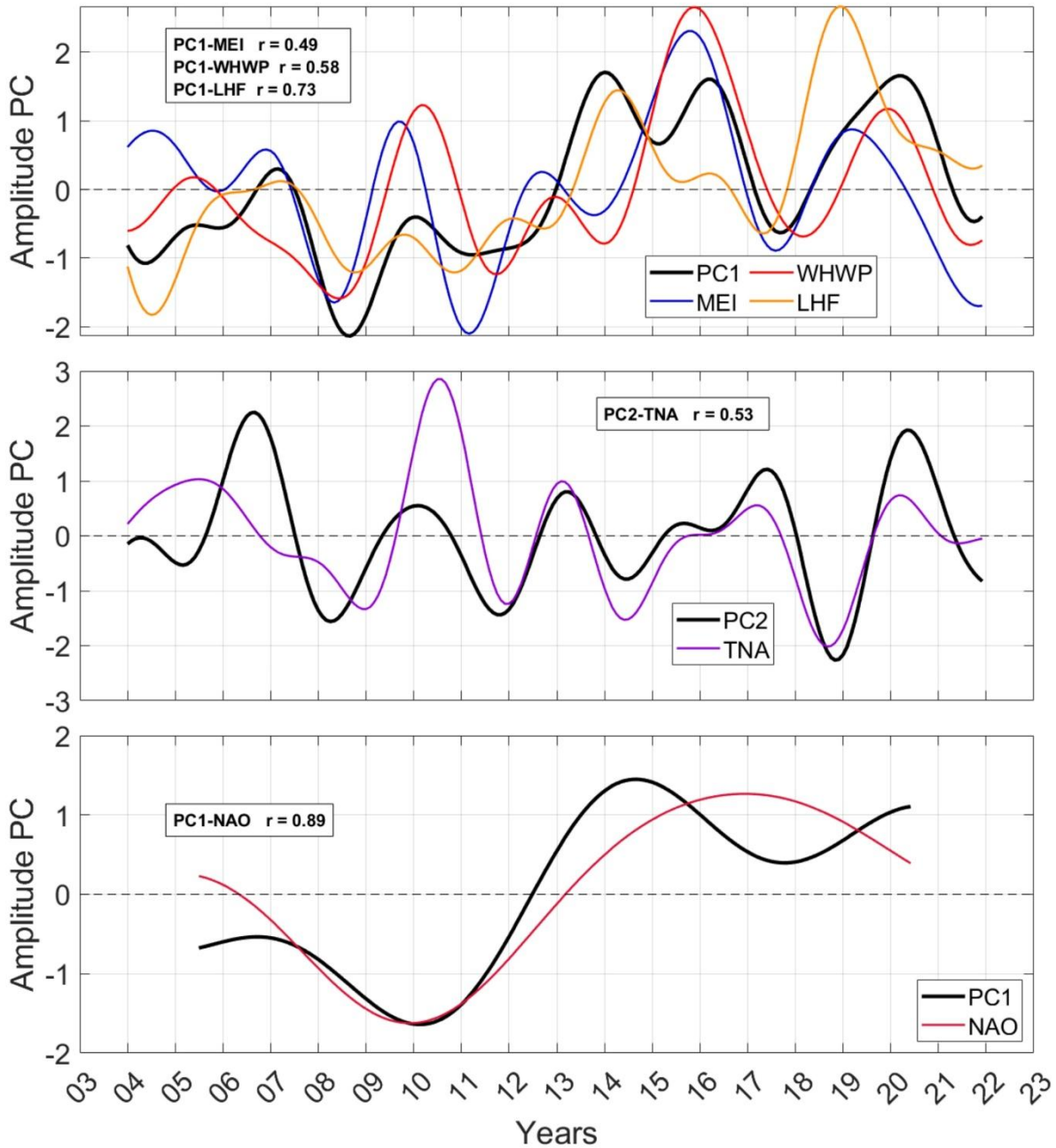
843

844

845

846

**Figure 9.** EOF analysis of monthly SST anomalies for 2003–2022. Left: spatial patterns of EOF1 (87.5 %) and EOF2 (6.2 %). Right: Corresponding principal components (PC1, PC2); thick black curve represents a two-year low-pass filter to emphasize interannual variability. (PC signs are arbitrary and chosen so that positive PCs correspond to warm anomalies in EOF1).



847

848 **Figure 10.** Co-variability of SST principal components (PCs) with climate drivers. (a) Interannual band: 2-year  
849 running-mean low-pass of PC1 (black) plotted with MEI.v2 (blue), Western Hemisphere Warm Pool (WHWP)  
850 (red), and domain-mean latent heat flux (LHF) from ERA5 (orange). (b) Interannual band: PC2 (black) with  
851 Tropical North Atlantic (TNA) (magenta). (c) Low-frequency band: 5-year running-mean low-pass of PC1  
852 (black) with North Atlantic Oscillation (NAO) (red). Numbers in text boxes denote zero-lag Pearson  
853 correlations ( $r$ ) computed on the filtered monthly series. Significance is evaluated using effective degrees of  
854 freedom (Section 2.5). Series are standardized.